

Supernematic

Dan Mao^{1, 2, 3} and Eun-Ah Kim^{1, 4}

¹*Department of Physics, Cornell University, Ithaca, NY, USA*

²*Department of Physics, University of Zürich, Winterthurerstrasse 190, 8057 Zürich, Switzerland*

³*Condensed Matter Theory Group, PSI Center for Scientific Computing, Theory and Data, Paul Scherrer Institute, 5232 Villigen PSI, Switzerland*

⁴*Department of Physics, Ewha Womans University, Seoul, South Korea*

Quantum theory of geometrically frustrated systems is usually approached as a gauge theory where the local conservation law becomes the Gauss law. Here we show that it can do something fundamentally different: enforce a global conserved quantity via a non-perturbative tiling invariant, rigorously linking microscopic geometry to a new macroscopically phase-coherent state. In a frustrated bosonic model on the honeycomb lattice in the cluster-charging regime at fractional filling, this mechanism protects a conserved global quantum number, the sublattice polarization $\tilde{N} = N_A - N_B$. Quantum fluctuation drives the spontaneous symmetry breaking of this global $U(1)$ symmetry to result in a supernematic phase — an incompressible yet phase-coherent quantum state that breaks rotational symmetry without forming a superfluid or realizing topological order. This establishes a route to a novel quantum many-body state driven by combinatorial constraints and boundary invariants. The realization of the SN on programmable quantum platforms can test ergodicity of the resonance operator in constrained quantum dynamics, and explore harnessing quantum hardware to explore classically hard tiling problems.

CONTENTS

I. Introduction	1	2. Symmetry properties under lattice transformations	18
II. Extended Hubbard model and the cluster charging regime	2	3. Relating coarse-grained fields to microscopic fields	18
III. Searching for new quantum number as a tiling problem	4	B. Sublattice density structure factor	20
A. Conway-Lagarias Invariant	5	C. Systematic construction of local operators	20
B. Quantum number for filling 2/3	7	1. Local operators in \mathbb{S}_{op}	21
IV. Three-colored double-dimer model	8	2. Zero operators	21
A. Microscopic mapping between particle occupation and dimers	8	D. Tile mapping and quantum number for filling 1/3	22
B. Coarse-grained height fields and their properties under lattice symmetries	9	E. Perturbing around trimer-RK point	23
C. Effective field theory description	10		
V. Columnar ordered phase	11	I. INTRODUCTION	
A. Zero temperature	11		
B. Finite temperature	11		
VI. Supernematic	12	Quantum systems at weak and strong coupling are governed by opposing organizing principles: kinetic energy favors delocalized, wave-like motion, while interaction energy drives particles toward optimal spatial organization.	
A. Zero temperature	12	Although the uncertainty principle complicates descriptions that bridge these regimes, each limit is often simple to characterize. In the weak-coupling limit, the system forms a delocalized momentum eigenstate. In the strong-coupling limit, interactions can stabilize a unique spatial arrangement through crystallization, as in the Wigner crystal[1] or the Mott insulator[2]. Yet when additional internal degrees of freedom or geometric constraints frustrate these interactions, the optimization problem admits a manifold of equally favorable configurations rather than a single solution. In such cases, even the classical limit becomes profoundly nontrivial, giving rise to emergent gauge structures that connect degenerate states, as exemplified by spin ice[3] and dimer models[4]. Understand-	
B. Finite temperature	14		
VII. Other fillings	15		
VIII. Summary and discussion	16		
References	17		
A. Details on symmetry properties of the height fields	18		
1. Columnar ordering states	18		

ing how quantum fluctuations navigate this degenerate landscape—whether they select an ordered phase or preserve the imprint of frustration—remains one of the most conceptually challenging problems in modern quantum many-body physics.

The fate of geometric frustration under quantum fluctuations in known cases is typically analyzed through gauge theories representing local constraints as Gauss laws. While deriving such continuum theories from generic lattice Hamiltonians is not analytically tractable, perturbing away from exactly soluble models has been productive [5, 6]. When the gauge theory is deconfined, the resulting state could be topologically ordered [7]. However, one may ask whether there is an alternative, rigorous path for the intricate microscopic geometrical constraints to leave their fingerprint on a quantum ground state. In this paper, we provide one such example. We will prove that geometrical frustration on the lattice can give rise to qualitatively new long-wavelength behavior that escapes a conventional gauge-theoretic description, without resorting to numerical simulations or uncontrolled approximations.

Here we consider the effect of quantum fluctuations for bosons in a honeycomb lattice under cluster-charging interaction at commensurate fractional fillings (1/3, 2/3, 1, 4/3, and 5/3) as shown in Fig. 1 a) schematically. The strong coupling limit of this model, first inspired by the extended Wannier orbitals in twisted bilayer graphene[8], is equivalent to the problem of densely tiling triangles on faces of a triangular lattice[9]. Finding a tiling solution to a finite region with general tiles is a computationally hard problem, although we could leverage exact Bethe ansatz solution to predict the exponential degeneracy in the tiling solutions in this case.

In this paper, we study whether the degenerate configuration space of the complex optimization problem can impact the quantum ground state properties in the presence of finite quantum fluctuations. We find the powerful notion of tiling invariance by Conway and Lagrias [10] indicates an emergent quantum number for quantum dynamics within the constrained space of configurations. We predict new macroscopically coherent quantum ground state characterized by spontaneous breaking of the emergent $U(1)$ symmetry associated with the quantum number and discuss the properties of the new state. We describe the state as “supernematic” (SN), emphasizing that quantum fluctuations within the degenerate manifold favor anisotropic resonating units, whose spontaneous orientational alignment breaks the C_3 point-group symmetry.

The rest of the manuscript is organized as follows. In Sec.II, we introduce the cluster charging model and discuss the smallest resonating operator which has anisotropic shape (See Fig.1b). In Sec.III, we prove the exactness of the emergent quantum number $\tilde{N} \equiv N_A - N_B$, the sublattice polarization, for the manifold satisfying cluster-charging constraints at a filling 2/3 of the honeycomb lattice. We do this by mapping the con-

figurations in the constrained Hilbert space to a tiling problem with a fixed tile set and using the Conway-Lagrias boundary invariant in Ref.[10]. In Sec. IV, we derive the effective field theory that can address the quantum phase transition associated with the spontaneous symmetry breaking of the emergent $U(1)$ symmetry. This is done through mapping the microscopic problem to a three-colored double-dimer model and then using the height-field representation of the dimer model. The resulting field theory describes a problem with intertwined orders with fields transform non-trivially under the emergent $U(1)$ symmetry, the lattice translation and the C_3 point group symmetry. We predict a continuous transition between a columnar-ordered phase (CO) that breaks translational symmetry and C_3 point-group symmetry (See Fig.1c), and a new macroscopically phase-coherent phase, which breaks the emergent $U(1)$ symmetry and the C_3 point-group symmetry, but not the lattice translation (See Fig.1d). Hence, we refer to this new phase as supernematic (SN). In Sec.V we discuss the properties of the columnar ordered phase and its melting via thermal fluctuations. In Sec.VI we discuss the properties of the supernematic phase and its thermal melting. The thermal phase diagram is summarized in Fig. 1e). In Sec.VIII, we summarize our results and discuss the implications.

II. EXTENDED HUBBARD MODEL AND THE CLUSTER CHARGING REGIME

Consider an extended Hubbard model on the honeycomb lattice, with bosonic (or spinless fermionic) degrees of freedom on the sites. In general, the Hamiltonian for such system can be written as,

$$H = \sum_{i,j} V_{(ij)} n_i n_j + \sum_{i,j} t_{ij} b_i^\dagger b_j, \quad (1)$$

where $V_{(ij)} = V_0, V_1, V_2, \dots$ denotes the interaction between particles of the same site, nearest neighbor, next nearest neighbor, etc (see Fig.1 a)). We always assume the hard-core condition, i.e. $V_0 \rightarrow \infty$.

The cluster-charging interaction of interest H_U represents an intermediate-range interaction in the form of

$$H_U = U \sum_r \left(\sum_{i \in \mathcal{O}_r} n_i \right)^2, \quad (2)$$

where the n_i is summed over the sites of an hexagonal plaquette labelled by r , and the interaction is summed over all honeycomb plaquettes. Expanding H_U in terms of density-density interaction, $4U = V_1 = 2V_2 = 2V_3$. This interaction is longer ranged than the on-site interaction of the Hubbard model, but it is not infinite-ranged like the Coulomb interaction. It has been shown that H_U introduces non-trivial orbital geometrical frustration, resulting in extensively degenerate configurations and local $U(1) \times U(1)$ gauge symmetry [9, 11, 12] in the classical

strong coupling limit. This intermediate-range interaction can arise when the interaction strengths in the general Hamiltonian Eq.1 follow a specific hierarchy. For the commensurate cases with filling 1 and 2/3 particles per unit cell, H_U dominate when $\max\{V_1, \frac{V_2}{2}, \frac{V_3}{2}\} \gg |V_1 - \frac{V_2}{2}|, |V_1 - \frac{V_3}{2}|, |V_2 - V_3|, V_k, W$, where $k \geq 4$ denotes the further range interaction, and W denotes the bandwidth. For filling 1/3, H_U dominate when $V_{1,2,3} \gg V_k, W$.

In Ref.[13], we showed that the classical ground state in the strong coupling limit of H_U is the so-called “trimer liquid” state, which is an ensemble of equal probability of all the possible particle configurations that minimize H_U . The trimer liquid has power-law correlation functions and pinch-point structure factor of particle density. The question we would like to address is the fate of trimer liquid under *bosonic quantum fluctuations* in the cluster-charging regime. We will primarily focus on filling of 2/3 particle per hexagonal plaquette and discuss generic commensurate fillings in Sec. VII.

There are several differences between the cluster-charging regime of interest and two better-known strongly interacting quantum bosonic models: the Bose Hubbard model and the extended Bose Hubbard model. With the extremely short-ranged interaction of the Hubbard model, the strong coupling limit is atomic, where each site can host zero or one bosons, subject to the total fillings. Quantum fluctuation introduced through hopping drives superfluidity, resulting in the well-known phase diagram [14] with “Mott-lobes” anchored by integer fillings with superfluid phase in-between, in terms of chemical potential versus hopping strength. With the further-range interaction of the extended Bose Hubbard model, quantum fluctuation usually gives rise to superfluid or supersolid phases where both break the $U(1)$ symmetry associated with the total particle number. However, such phase coherence is forbidden for the cluster-charging Hamiltonian ground state since the total particle number is related to the sum of the cluster-charging over all the plaquettes, which are local gauge symmetries. By Elitzur’s theorem [15] the usual $U(1)$ symmetry no longer can be broken spontaneously, guaranteeing a correlated insulating state for our model. Now, the question is: what else can happen to the quantum ground state of the model?

The first step for considering the effect of quantum fluctuation in geometrically frustrated problems is to identify the minimal resonating operator that connects different configurations and the symmetry these operators may preserve. In the canonical example of the dimer model, the effect of quantum fluctuations is wildly different between the bipartite and non-bipartite lattices. The local resonating operators admit a $U(1)$ gauge structure for bipartite lattice while a Z_2 gauge structure for non-bipartite lattice [4, 16]. Due to the confinement of the compact $U(1)$ gauge theory in $2+1D$ [17], the quantum dimer model on a bipartite lattice has gapped ground states that usually break lattice translational symmetry. On the other hand, the quantum dimer model on a non-

bipartite lattice can have a gapped topologically ordered state, which is the deconfined phase of the Z_2 gauge theory [18] [19].

In the cluster-charging regime, the local resonating operators depend on the filling fraction. For the filling of 2/3, the operator involving the smallest number of nearest neighbor hopping is the operator we denote as \mathcal{O}_2 in Fig.1c), because a smaller resonating operator involving only one plaquette annihilates all the states in the constraint space (see Appendix Sec.C for the derivation). There are significant consequences to the extended local structure of the \mathcal{O}_2 taking the elongated shape (a similar scenario for filling 1/3, which is called “lemniscate” in Ref. [12], also discussed in Sec.VII). Firstly, the elongated shape means that the resonant fluctuation can occur locally in three different orientations, $\alpha = 1, 2, 3$. Secondly, the resonating operator \mathcal{O}_2 locally shuffles the sublattice polarization between the two neighboring plaquettes supporting the \mathcal{O}_2 operator. Hence, in the cluster-charging regime of filling 2/3, the effective Hamiltonian can be written as

$$\mathcal{H} = -t_2 \sum_{i,\alpha} \mathcal{O}_2^\alpha(x_i) + h.c. + H_U + V_0 \sum_i n_i^2 + \dots, \quad (3)$$

where α denotes the different orientation of the \mathcal{O}_2 operator and H_U refers to the cluster charging interaction in Eq. (2), which is a constant that can be dropped. We include the on-site Hubbard term proportional to V_0 to impose the hard-core condition, and the \dots to denote higher order ring-exchange operators and other density-density interactions.

We are interested in the phases of the quantum Hamiltonian \mathcal{H} under finite quantum fluctuation t_2 and interactions. The emergent $U(1) \times U(1)$ gauge structure we found earlier in the classical limit by mapping the classical model to coupled dimer models (see Ref. [12] Appendix F, also see Sec.IV) carries over to the quantum Hamiltonian \mathcal{H} . If the local $U(1) \times U(1)$ symmetry were to be the only conservation law in the problem, one would expect quantum fluctuations to drive confinement and a gapped spectrum as in the quantum dimer model on a bipartite lattice. However, as we will show in the next section, the \mathcal{O}_2 operator globally preserves an additional quantum number: the sublattice polarization, $\tilde{N} \equiv N_A - N_B$, which will be proved to remain conserved under all local terms in \mathcal{H} . This conservation law is independent of the 1-form symmetry of the $U(1) \times U(1)$ gauge theory, indicating a richer structure beyond conventional confinement physics in quantum dimer models. The conservation of N suggests a possible spontaneous symmetry breaking phase with macroscopic phase coherence, analogous to a superfluid, coexisting with the confinement of the $U(1) \times U(1)$ gauge theory: the supernematic (SN). As we show later, the SN has two features: the spontaneous symmetry breaking of \tilde{N} conservation leads to gapless Goldstone mode and phase coherence, and the confinement of the $U(1) \times U(1)$ gauge field leads to the C_3 three-fold rotational symmetry breaking.

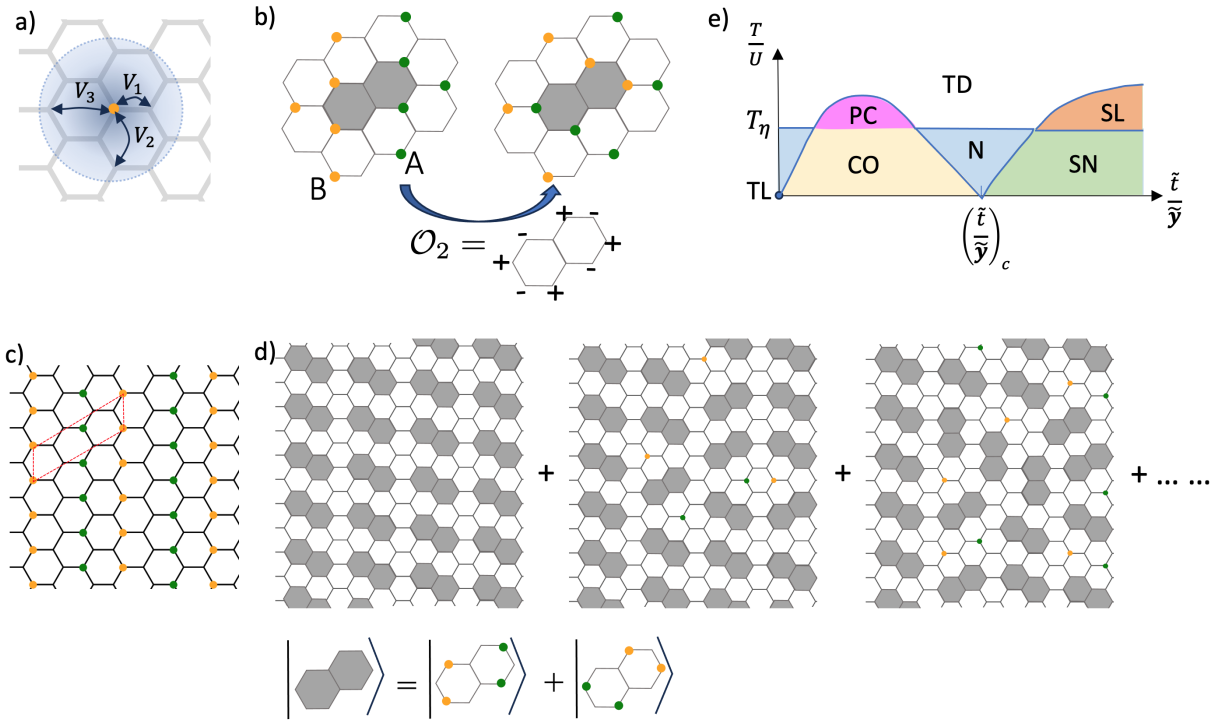


FIG. 1. a) The cluster charging model, with repulsive interaction upto third nearest neighbor. The blue shaded area denotes the range of the interaction. b) The smallest local move that changes the particle configuration locally, by applying the \mathcal{O}_2 operator, whose \pm signs denote particle creation/annihilation. c) The colomnar order with alternating colomns of occupation on A sublattices (green) and B sublattices (orange). The unitcell is indicated by the red dashed lines. d) Top: the schematic wavefunction of the resonating state, with superposition of various tilings of the local resonating patterns (grey double-plaquette). Bottom: the grey double-plaquette denotes a local resonance of the two configurations. e) Schematic phase diagram of the quantum model, where \tilde{t}/\tilde{y} is the tuning parameter (see Sec.IV C), and T_η denotes the transition temperature of the $\vec{\eta}$ -field, which is tuned by a different parameter of \tilde{t}/\tilde{y} . Here the T_η is picked such that all the thermal phases discussed in Sec.V B and Sec. VII B can be shown. For larger T_η , the area of PC and SL will shrink and these phases can disappear. TL: “trimer liquid”, which is the extensively degenerate classical ground state satisfying cluster-charging contraintes. CO: “colomnar ordering” (panel b)). PC: plaquette Coulomb. N: Nematic phase. SL: “Super”-fluid. SN: Supernematic (panel d)). TD: thermally disordered. The quantum phase transition between CO and SN at zero temperature is of 3D XY universality class. The blue lines denote the thermal phase transition of the three-state Potts universality class.

III. SEARCHING FOR NEW QUANTUM NUMBER AS A TILING PROBLEM

We seek the quantum number that is preserved under local resonating dynamics (Fig.1b) and higher order terms) by mapping the problem of allowed particle configurations to the problem of tiling. Tiling problems are a class of combinatorial problems generally considered NP-hard. The rule of the game is to cover a given bounded region with certain geometric shapes, i.e., the tiles, such that the tiles neither overlap nor have gaps in between. The seminal work of Conway and Lagarias [10] shifted the focus from finding a tiling solution to establishing a no-go theorem of tiling impossibility: tiling is impossible when boundary invariants associated with the tile set are violated, where the boundary invariants are derived using the language of combinatorial group theory. As we will make precise in the following, such a boundary invariant can lead to a new quantum number when dynamics

is restricted to configurations satisfying cluster-charging contraints at filling 2/3.

To make the mapping between tiling and particle configurations at filling 2/3, we first consider miniature tiles that are smaller than the original honeycomb plaquettes (shapes with green and magenta contours in Fig.2a). The intuition is to imagine “blowing up” each particle so that it acquires a geometric shape, with none of the shapes overlapping. Equivalently, we can view the tiling pattern as emerging from joining together the “puzzle” pieces, where each piece is the physical hexagonal plaque decorated with magenta and green lines. We can now approach the resonant of Fig.1c) as two allowed tiling configurations where only a subset of the miniature tiles are rearranged (Fig.2b)).

Now, to further connect to the original problem considered in Ref.[10], we view the bigger tiles with the green/magenta contours in Fig.2 as consisting of the smaller three-in-line tiles and triangular tiles of three co-

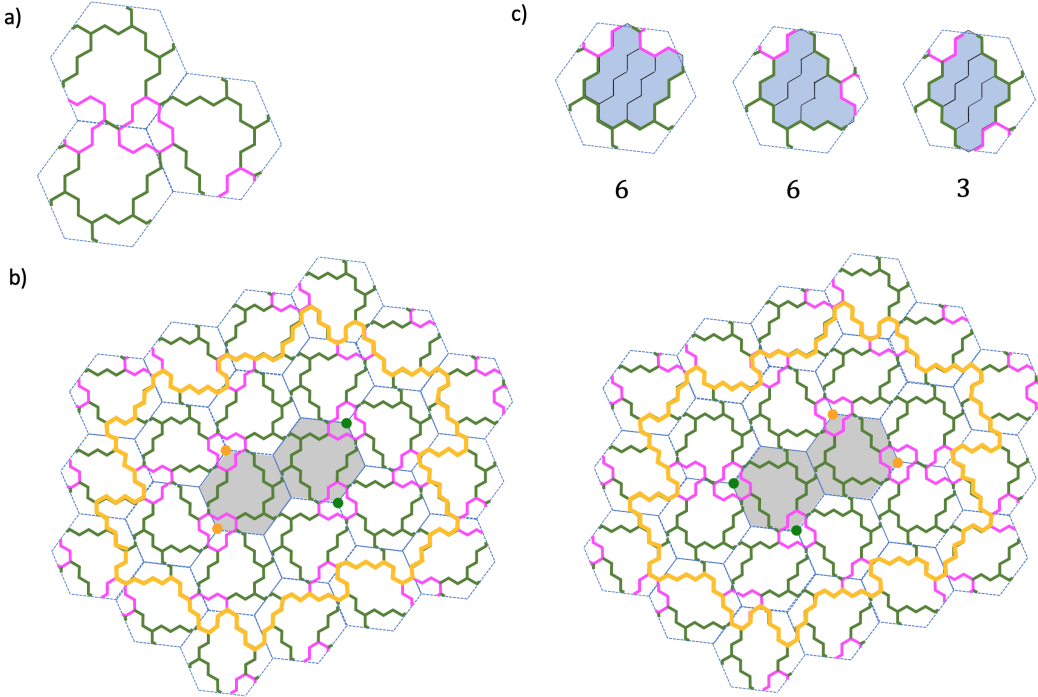


FIG. 2. a) A mapping between particle configuration and tiling pattern with miniature tiles. The magenta-contoured triangular tiles maps to the sites with particle occupation. The green-contoured and mixed-color-contoured tiles map to the holes and the spaces in between particles and holes. b) The tile mapping of the configurations in a), with the same blue shaded region. The yellow line marked the boundary where the change of the configuration is contained, and the shape of the boundary remain intact under the flipping move. The grey shades and the orange and green dots mark the corresponding configuration in Fig.1 b). c) The exact mapping between all the possible particle configurations of each plaquette (puzzle pieces) and the tiling pattern. There are 15 different configurations (choosing 2 out of 6). The number underneath each plaquette denotes all the configurations related by C_6 rotation. The blue shades denote the decomposition of a bigger tile into small tiles. Note that there can be multiple possible decompositions but all of them consist of tiles given in Fig.3 a) and b).

joining plaquettes (blue shades in 2c). All the allowed particle configurations can therefore be mapped to tiling patterns by connecting the hexagonal pieces in Fig.2c) in a boundary-matching way. The sites with particles are mapped to magenta tiles. Note that all the tiles fall into the tile sets in Fig.3a) and b).

For these tiles, the following theorem proved in Ref.[10] connects allowed tiling configurations to a boundary invariant.

Theorem 1 (Conway-Lagarias). *For any simply connected region R , if R is tilable by Σ_1 (Fig.3 a) and Σ_2 (Fig.3 b), we can define a boundary invariant $\phi([\partial R])$. On the one hand, $\phi([\partial R])$ only depends on the boundary of R , denoted as ∂R . On the other hand, $\phi([\partial R]) = \sum_{i \in R} \phi([\partial T_i])$, where T_i is the tile contained in R , and $\phi([\partial T_1]) = 1$, $\phi([\partial T_2]) = -1$, and $\phi([\partial T_{3,4,5}]) = 0$.*

Here, tilability means there are no gaps or overlaps between the tiles, which corresponds to satisfying the cluster charging constraints while fixing the filling to 2/3 particles per unit cell. In the remainder of this section, we first give a pedagogical proof of Thm.1 for completeness and then show that the tiling invariance rigorously establishes a new emergent quantum number for the quantum

cluster-charging Hamiltonian of Eq. (3).

A. Conway-Lagarias Invariant

To construct the boundary invariant in Thm.1, Ref.[10] maps the boundary of the tiling to another “space”, where the boundaries of the different tiling types carry different winding numbers.

First, we need an algebraic description of the tiles and the tiling problem. The relevant tile set for 2/3-filling (Fig.2) can be classified into two sets, triangular set Σ_1 (Fig.3a) and three-in-line set Σ_2 (Fig.3b). It turns out to be convenient to view the tiles T_i as tiles on the square lattice by “shrinking” along one orientation of the bonds on the honeycomb lattice, as illustrated in Fig.3a and b. We glue the two sites connected by the orange bonds on the honeycomb lattice and reshape the remaining edges to be horizontal and vertical to obtain the corresponding tiles on the square lattice, which are called “polyominoes”.

Then, we need to characterize different “shapes” of the tiles. One way to achieve this is to describe the paths along the boundary of the tiles by the words (elements)

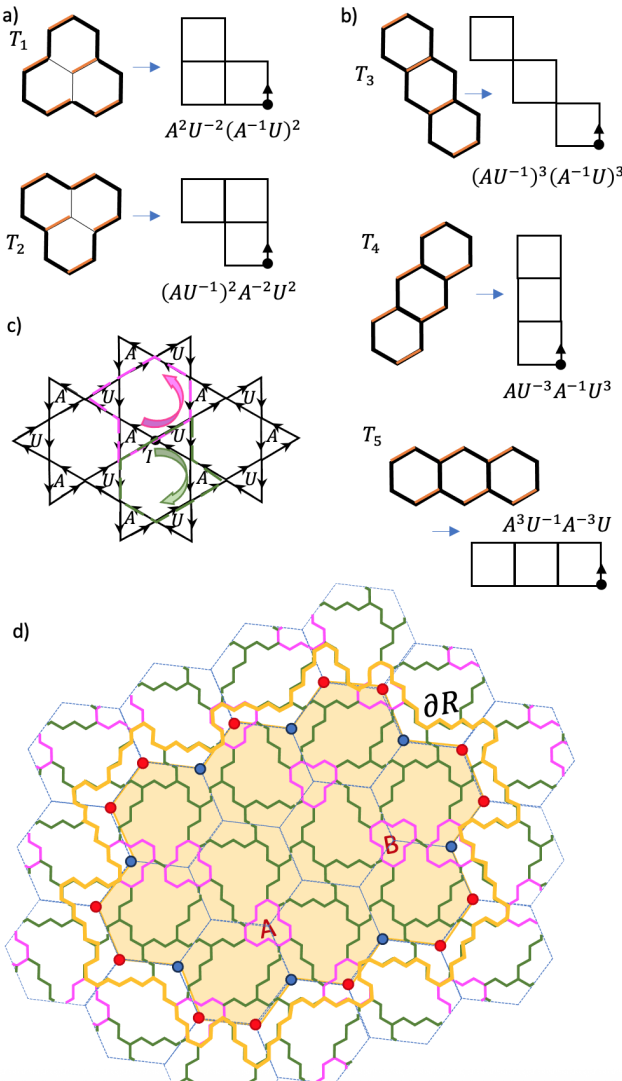


FIG. 3. a) Triangular tile set Σ_1 and b) three-in-line tile set Σ_2 . The black dots label the base points for the paths that generate the words written below. c) Cayley graph, where the magenta and green loops correspond to the paths of ∂T_1 and ∂T_2 , with the arrows indicating the direction of the paths. d) Taken from Fig.2c. The orange line denotes the defined boundary ∂T for a region that consists of orange-shaded plaquettes. The magenta tiles denote the particle occupation, with A and B sublattices labeled. The sites on the boundary of the orange-shaded region belong to either S_2 (blue dots) or S_1 (red dots), depending on whether they lie in two or one hexagonal plaquettes of the orange region of interest.

in free group. On the square lattice, we consider a free group $F = \langle A, U \rangle$, where A and U are the two generators, denoting going right and going up. Next, we fix a base point \vec{e}_i on the boundary of a tile T_i , and denote the “word” generated by going along the boundary counter-clockwise as $\partial T_i(\vec{e}_i)$, with the corresponding generators multiplied to the left. We call this *oriented boundary* of T_i . For example, the oriented boundary of T_1 can be written as $\partial T_1(\vec{e}_1) = A^2U^{-2}(A^{-1}U)^2$ (see Fig.3a and b for

other ∂T_i ’s). It is readily seen that if we choose a different base point on the lattice, say \vec{e}'_i , the oriented boundary $\partial T_i(\vec{e}'_i)$ would be the conjugate of the previous word, and can be written as $W^{-1}(\partial T_i(\vec{e}_i))W$, where $W \in F$. Hence, for any simply connected region R_s , it is convenient to define the *combinatorial boundary* of R_s as the conjugacy class in F that contains all the oriented boundaries $\partial R_s(\vec{e})$ ’s, that is $[\partial R_s] = \{W^{-1}\partial R_s(\vec{e})W, W \in F\}$.

Now we join the tiles to form a tiling pattern. First if one joins two tiles T_i and T_j , the boundary word of the joined region can always be written as $W_i^{-1}(\partial T_i(\vec{e}_i))W_iW_j^{-1}(\partial T_j(\vec{e}_j))W_j$, with $W_{i,j} \in F$. We can then proceed to put more tiles together. Eventually, we observe that for any simply connected tilable region R , its boundary word can always be decomposed into boundary words of the single tiles inside R , that is,

$$\partial R = \prod_{i \in R} W_i^{-1}(\partial T_i(\vec{e}_i))W_i. \quad (4)$$

In the above equation, the l.h.s. depends only on the path along the boundary ∂R , whereas the r.h.s. depends on the ∂T_i ’s, which in turn depend on the tiles inside the region R . The W_i ’s contain information of how these tiles glue together. Hence, we can define *tile group* $T(\Sigma)$ as

$$T(\Sigma) = N(\langle \partial T_i(\vec{e}_i) \rangle), \quad (5)$$

where $N(\dots)$ denotes the normal subgroup in F . From our previous argument, if R is tilable by Σ , $\partial R \in T(\Sigma)$.

Next, in order to find the so-called boundary invariant, we only need to find a homomorphism between the tile group and integers. We achieve this by first finding a larger group H that contains the tile group $T(\Sigma)$.

$$H = N(\langle A^3, U^3, (U^{-1}A)^3 \rangle). \quad (6)$$

The presentation of H is less important to us since we will work with the Cayley graph $\mathcal{G}(F/H)$ in the following. The Cayley graph $\mathcal{G}(G)$ is a graph with directed edges for visualizing the structure of the group G . We define the identity element I as the origin of the graph. For each vertex, the outgoing edges denote the generators of the group and the ingoing edges denote their inverses. The Cayley graph $\mathcal{G}(F/H)$ is shown in Fig.3c, which is a Kagome lattice. The edges are labeled with the generators A and U . Let us consider a directed path on the graph and define the following rule: If the path’s direction matches the edge it crosses, the corresponding generator is multiplied; otherwise, the inverse of the generator is multiplied. Following this rule, we can map elements in $T(\Sigma)$ to paths on the Cayley graph in Fig.3c. Since $T(\Sigma) \subset H$, these paths are closed loops, as the magenta and green loops shown in Fig.3c.

For a directed close path L on the Cayley graph, we can always define the winding number $\phi(L)$ to be the number of counterclockwise loops around the hexagonal

cells enclosed by the closed directed path L . In particular, we find that for the combinatorial boundaries of the tiles, $\phi([\partial T_1]) = 1$, $\phi([\partial T_2]) = -1$, and $\phi([\partial T_{3,4,5}]) = 0$. It is straightforward to show that ϕ is a homomorphism by showing $\phi(AB) = \phi(A) + \phi(B)$, for $A, B \in T(\Sigma)$. Combining the definition of ϕ and Eq.4, it is readily seen that for any tilable region R ,

$$\phi([\partial R]) = \sum_{i \in R} \phi([\partial T_i]) \quad (\text{Thm.1}). \quad (7)$$

B. Quantum number for filling 2/3

Thm.1 by itself is a statement regarding each individual tiling patterns, which we have mapped to the particle configuration at filling 2/3. In the following, we will show that Thm.1 indeed gives rise to a conservation of the total sublattice particle number difference, $N_A - N_B$, which should be thought of as a good quantum number of a generic local Hamiltonian acting within the constrained Hilbert space. The same conclusion also holds for filling 1/3 and the proof is given in App.D.

To connect the winding number $\phi([\partial R])$ in Thm.1 to physical quantities, consider an arbitrary simply connected region, for example, the orange shaded region in Fig.3d). Any particle configuration in the classical ground state of H_U at the fixed filling maps to a proper tiling of the region with the tile set $\{T_1, \dots, T_5\}$ shown in Fig.3a)-b) where the particles map to T_1 and T_2 marked in magenta, and the space between particles maps to regions with green/magenta contours which can be built with the full tile set $\{T_1, \dots, T_5\}$ as shown in Fig. 2c). To apply Thm.1, we need to define the boundary of the region carefully. The tiling boundary ∂R (yellow line) is naturally defined as the outer contour of the magenta and green tiles covering the physical lattice sites along the boundary of the region of interest. Some sites touch only one physical plaquette in the region of interest. These sites form the set S_1 and are marked in red. Some sites touch two physical plaquettes in the region of interest. These sites form the set S_2 and are marked in blue. Now we can apply the Thm.1 to the tiling boundary ∂R , to find the CL tiling invariance for the tile set $\{T_1, \dots, T_5\}$:

$$\phi([\partial R]) = (N_{T_1} - N_{T_2})_R, \quad (8)$$

where the right hand side is the number of T_1 tiles minus the number of the T_2 tiles within the region R . The simplicity emerges from the winding number of the tiles $T_{3,4,5}$ being zero, i.e., $\phi([\partial T_{3,4,5}]) = 0$.

To use the CL invariance Eq. (8) to derive a global quantum number for the Hamiltonian \mathcal{H} at filling 2/3, we need to deal with the complexity arising from the “puzzle” pieces being composites including T_1 and T_2 tiles. While T_1 and T_2 tiles marked in magenta in Fig. 3d) correspond to A and B sublattice site occupation, respectively, T_1 and T_2 inside the green tiles do not correspond

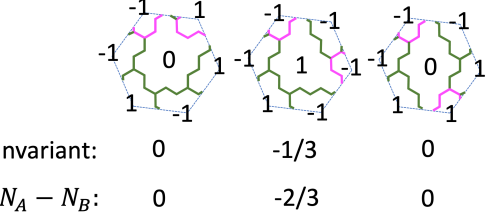


FIG. 4. Assignment of the “puzzle” invariant Φ_p for three configurations. The integers denote the boundary invariant of the corresponding regions. The invariant of the puzzle piece is calculated by summing the middle number and 1/3 of the numbers at the boundary. The “ $N_A - N_B$ ” row denotes 1/3 of the total particle occupation $N_A - N_B$ of the above hexagon, magenta tiles being the locations of the physical particles. Here only the puzzle with $N_A = 0, N_B = 2$ is shown, the piece with $N_A = 2, N_B = 0$ can be obtained by a 60° rotation of the former one, giving $\Phi_p = 1/3$.

to physical particles. To carefully deal with the complexity, we assign a “puzzle” invariant Φ_p to each of the fifteen puzzle pieces by summing two contributions: (i) the boundary invariant in the middle region and (ii) one-third of the boundary invariants of the tiles surrounding the vertices of the hexagon (see Fig. 4). Here, we use the CL invariance Eq. (8) to calculate the boundary invariant of each of the tiles. As shown in Fig. 4, each particle occupying the A (B) sublattice contributes +1/6 (-1/6) to Φ_p .

Now we can use Thm. 1 to relate the boundary invariant ∂R to a sum of puzzle invariants for the puzzles enclosed in the region R and the boundary tile contributions as

$$\phi([\partial R]) = \sum_{i \in R} \Phi_p(i) + \frac{2}{3} \sum_{i \in S_1} \phi_i + \frac{1}{3} \sum_{i \in S_2} \phi_i, \quad (9)$$

where ϕ_i denotes the winding number of the tiles at the site i on the boundary. Next, we observe the relationship between the puzzle invariants and the sublattice polarization $\tilde{N} \equiv N_A - N_B$. While $\frac{1}{3}\tilde{N}$ can be $\{-2/3, 0, 2/3\}$ for each plaquette p , corresponding Φ_p are $\{-1/3, 0, 1/3\}$ as depicted in Fig. 4. Hence summing over Φ_p within region R contains summing over $\frac{1}{2}\tilde{N}$ in the interior since each vertex is touched upon three times by the hexagonal plaquettes. At the boundary, however, how many internal plaquettes in the region R share the particles (the magenta tiles) depends on which set the boundary site i belongs to. When the site i is in S_1 (red), the magenta tile is touched by only one internal plaquette, and the counting from summing over Φ_p misses a factor of $\frac{1}{3}$. On the other hand, when the site i is in S_2 (blue), the magenta tile is touched by two internal plaquettes, and the missing factor is $\frac{1}{6}$. Hence we arrive at the full counting of the sublattice polarization of the region R (including

both the interior and the boundary) as

$$\frac{1}{2}(N_A - N_B)_R = \sum_{i \in R} \Phi_p(i) + \frac{1}{3} \sum_{i \in S_1} \phi_{i,M} + \frac{1}{6} \sum_{i \in S_2} \phi_{i,M}, \quad (10)$$

where $\phi_{i,M}$ denotes the winding number of the magenta tiles enclosing site i on the boundary.

Now we can eliminate the Φ_p terms between Eqs. 9 and 10 to obtain the first major result of this paper:

$$\begin{aligned} & \frac{1}{2}(N_A - N_B)_R \\ &= \phi([\partial R]) - \frac{2}{3} \sum_{i \in S_1} (\phi_i - \frac{1}{2} \phi_{i,M}) - \frac{1}{3} \sum_{i \in S_2} (\phi_i - \frac{1}{2} \phi_{i,M}). \end{aligned} \quad (11)$$

The left-hand side of Eq. 11 is a purely “bulk” physical quantity determined by the configuration within region R , while the terms on the right-hand side are boundary contributions. In the sense that there is a bulk charge that can be related to the boundary properties, the relationship is reminiscent of topological invariants. However, unlike topological invariants with underlying gauge theory, the $\tilde{N}_R \equiv (N_A - N_B)_R$ depends on the shape of the boundary. Instead, Eq. 11 implies a conserved global quantum number associated with the total $\tilde{N} = N_A - N_B$. To see this, consider any local operator \mathcal{O} with finite support in an infinite system. We can always choose a region R that fully encloses the support of \mathcal{O} such that its action leaves the boundary configuration unchanged. Consequently, acting with \mathcal{O} does not modify the right-hand side of Eq. 11, implying that the sublattice particle number within R is conserved from the left-hand side. Since \mathcal{O} acts only inside R , the configuration outside R remains unaffected, and thus the total \tilde{N} in the system is conserved. Although the precise support of \mathcal{O} and the corresponding choice of R may vary, as long as \mathcal{O} remains local (its support does not scale with system size), one can always identify a suitable region R satisfying the above condition. Since \mathcal{O} redistributes \tilde{N} locally, only the total \tilde{N} is conserved, making \tilde{N} a distinct global symmetry rather than the local conservation following from the cluster-charging constraints. Hence, for any effective Hamiltonian \mathcal{H} acting on the constrained Hilbert space with local terms, the global quantity \tilde{N} is a good quantum number.

IV. THREE-COLORED DOUBLE-DIMER MODEL

Previously we showed that, at filling 2/3 within the constrained Hilbert space, the sublattice imbalance $\tilde{N} \equiv N_A - N_B$ emerges as a conserved $U(1)$ charge. Taking into account this emergent symmetry with the lattice symmetry allows us to derive an effective field theory, starting from the mapping of the quantum Hamiltonian to a three-colored double-dimer model. The resulting

field theory has two phases: the columnar ordering phase (CO) and the supernematic phase (SN).

A. Microscopic mapping between particle occupation and dimers

The cluster-charging constraints can be recast into the more familiar constraints in dimer models by viewing the particle as three conjoined dimers. We used this mapping in Ref.[13] to derive the 2D statistical field theory for the classical cluster-charging model at filling 1/3, where only two height fields are independent at long wavelength since the fluctuations around the constraint relating the three height fields are irrelevant in the classical theory. We now generalize this mapping to filling 2/3 and consider the effect of quantum fluctuations. Quantum theory lives in 2+1D, and we will find three independent height fields because the quantum fluctuation of the constraint is gapless.

First, we view the dual lattice of the physical honeycomb lattice as a set of three interpenetrating honeycomb lattices, labelled as red, green, and blue in Fig.5 a). We then map the particle occupation to three dimer occupations (red, blue and green dimers in Fig.5 a)). The mapping between the dimer occupation and physical particle number can be written as $d_a^r = n_i + n_j$, where d_a^r denotes the “red” dimer occupation number at bond a and $n_{i,j}$ are the particle numbers at site i, j , which are the sites linked by the edge of the physical lattice intersected with bond a , as noted in Fig.5 b). The analogous expressions also hold for the green and blue lattices. At filling 2/3, the cluster-charging constraints impose “two-dimers per site” conditions on the colored honeycomb lattice with double-occupation of dimers allowed (illustrated in Fig.5 b) for the red lattice). The corresponding dimer model of each colored honeycomb lattice is the so-called “double-dimer” model, because the configuration can be thought of as overlaying two dimer coverings with one dimer touching each vertex [20].

Now we introduce the height fields. In the dimer model, height fields are integer-valued fields defined at the centers of the plaquettes to encode the dimer constraints [21, 22]. Since the double-dimer configuration can be decomposed into two single-dimer ones, Ref. [23] introduces two height fields for each of the replicas. Here, for the cluster-charging model, only the sum of the two heights is relevant since no physical operators can distinguish the two replicas. We will call this summation “the height field” in the following. The height fields of the red double-dimer model are defined at the centers of the hexagonal plaquettes, with the following rules (Fig.5 c)): when going around the vertex emitting “Y” shaped edges clockwise, if no dimer/one dimer/two dimers is crossed, height is changed by $-2/+1/+4$. The height assignment is the same for going around another type of sublattice counter-clockwise. Under such rules, the action of the \mathcal{O}_2 operator is to shift the height field of one color by -3 and

the height field of another color by $+3$ (Fig. 5 d)). Now the total $\tilde{N} \equiv N_A - N_B$ conservation proved in section III maps to the global conservation of the total height fields $h_r + h_g + h_b$.

We now express the Hamiltonian of our cluster charging model Eq. 3, in terms of the heights h_l^r and its canonical conjugate θ_l^r with $[\theta_l^r, h_{l'}^r] = i\delta_{ll'}$, where l, l' label the sites and r labels the color. The hopping-induced quantum fluctuation associated with the resonance operator \mathcal{O}_2 can be written as,

$$H_t = -t_2 \sum_{l,\alpha} \cos(3\theta_l^r - 3\theta_{l+\alpha}^g) + (\text{permutation of colors}), \quad (12)$$

where $l, l + \alpha$ label the center of the hexagonal plaquette at position l and its neighbor. Since different colors reside in different sublattices, we will drop the color label for simplicity. For visual purpose, sometimes we color the hexagonal plaquettes to remind ourselves of the coloring of the height fields defined at center of the plaquettes (Fig. 5 b)).

To map the density-density interaction to heights, we first express the particle occupation in terms of the height fields (upto a constant shift of the height field of the same color, which we have fixed),

$$n_A = -\frac{1}{3} \sum_{\triangleright} h + \frac{1}{3}, \quad n_B = \frac{1}{3} \sum_{\triangleleft} h + \frac{1}{3}, \quad (13)$$

where the $\triangleright/\triangleleft$ is the shorthand notation for summing the three height fields surrounding the site of the corresponding particle (see Fig. 5 e)), where the color labels are implicit. The constant $\frac{1}{3}$ takes care of the filling fraction. The representation of the particle number using the fields on dual lattice can also be viewed as a plaquette duality, utilized for studying various spin models with ring exchange interactions [24, 25]. The additional link to the height fields is originated from the cluster-charging constraints. Now, the on-site Hubbard term H_0 can be written as,

$$H_0 = V_0 \left[\sum_i \left(\sum_{\triangleright_i} h \right)^2 + \sum_j \left(\sum_{\triangleleft_j} h \right)^2 \right], \quad (14)$$

where i, j denote the A, B sublattice sites and $\triangleright_i, \triangleleft_j$ denote the three plaquettes surrounding these site, and the constant shift in Eq. 13 for A and B sublattices gives rise to a constant term that we drop. The density-density interaction beyond on-site terms can be expressed in a similar way.

B. Coarse-grained height fields and their properties under lattice symmetries

Now, let us focus on the limit where t_2 and V_0 are large. H_t favors configurations with a uniform θ -field for all

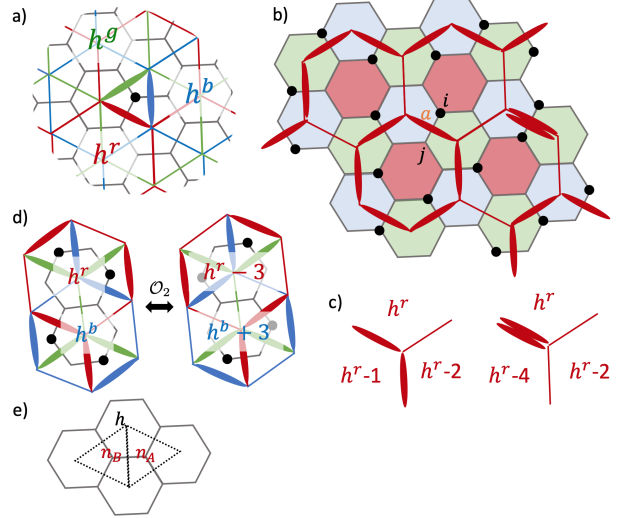


FIG. 5. Mapping between trimer model at 2/3-filling to the three-colored double-dimer model. a) Mapping between one particle and corresponding three dimers, with the height field defined at the plaquette centers of the corresponding colored honeycomb lattices. b) An example of particle configuration and the corresponding double-dimer covering (only red is shown). The three-coloring of the original hexagonal plaquettes denotes support for the height field of the corresponding color. c) Height field assignment of the double-dimer model. d) Height change induced by applying the local move operator \mathcal{O}_2 . e) Particle numbers on different sublattices (n_A and n_B) are related to the sum of the three height fields h (of different colors) around the sites indicated by the dashed lines.

the colors, while H_0 favors an alternating pattern of the height fields of three colors, due to the three-sublattice structure in the relationship between h and n . Therefore, the long wavelength behavior needs to capture fluctuations near both the Γ -point ($k = 0$) and the K -point ($k = (0, \frac{4\pi}{3})$) of the Brillouin zone:

$$\begin{aligned} \theta_l &\sim \theta_0(x_l) + \vartheta(x_l)e^{iK \cdot x_l} + \bar{\vartheta}(x_l)e^{-iK \cdot x_l} \\ h_l &\sim h_0(x_l) + \eta(x_l)e^{iK \cdot x_l} + \bar{\eta}(x_l)e^{-iK \cdot x_l}, \end{aligned} \quad (15)$$

with the conjugacy pairs (θ_0, h_0) and (ϑ, η) . Here h_0 is a real scalar field and η is a complex scalar field.

The h_0 and η fields are nothing but a parametrization of the $h^{r,g,b}$ fields. Namely,

$$\begin{aligned} h_l^r &\sim h_0(x_l) + \eta(x_l) + \bar{\eta}(x_l) \\ h_l^g &\sim h_0(x_l) + \eta(x_l)e^{-i\frac{4\pi}{3}} + \bar{\eta}(x_l)e^{i\frac{4\pi}{3}} \\ h_l^b &\sim h_0(x_l) + \eta(x_l)e^{i\frac{4\pi}{3}} + \bar{\eta}(x_l)e^{-i\frac{4\pi}{3}}, \end{aligned} \quad (16)$$

similarly for the relationship between $\theta^{r,g,b}$ and θ_0, ϑ and $\bar{\vartheta}$. Here we view h_0 and η as coarse-grained height fields. Due to the dimer constraints, the microscopic heights always fluctuate at the length scale of the lattice constant of the colored honeycomb lattice. Conceptually, the coarse-grained height fields h_0 and η are obtained by

smearing the fluctuations due to the dimer constraints, but the procedure is not relevant for us at this point. What we are interested in are the forms of physical operators in terms of the coarse-grained fields and their properties under lattice symmetries.

First, the compactification radius of $h^{r,g,b}$ is 3 for our double-dimer model, since the uniform shift by three gives the same dimer configuration (same as the dimer model on honeycomb lattice [26]). Therefore, the physical operators can only be $\partial h^{r,g,b}$ (and higher order derivatives), the vertex operators $\mathcal{V}_{\vec{m}}(x) = e^{i\frac{2\pi}{3}\vec{m}\cdot\vec{h}(x)}$, where $\vec{m} = (m^r, m^g, m^b)$ is a vector of integers and $\vec{h} = (h^r, h^g, h^b)$, and their combinations.

The transformation of the coarse-grained fields under lattice symmetries can be derived from the “flat” configurations of $h^{r,g,b}$ ’s. These are columnar orders of the double-dimer model. However, not all columnar order combinations are physical, since not all double-dimer configurations can be mapped to physical ones. There are nine physical columnar orders in total, related to the configuration in Fig.1 b) by lattice translations and rotations. The symmetry transformation of the coarse-grained height fields need to account for not only the symmetry properties of the microscopic heights, but also the transformation of the average height, analogous to the discussion of the dimer model [26, 27]. The detail is discussed in the Appendix Sec.A. We will quote the results below. Under lattice symmetry,

$$\begin{aligned} \mathcal{T}_1 : h_0(x) &\rightarrow h_0(x) - 1; \eta(x) \rightarrow \eta(x)e^{-i\frac{4\pi}{3}} \\ \mathcal{T}_2 : h_0(x) &\rightarrow h_0(x) - 1; \eta(x) \rightarrow \eta(x)e^{i\frac{4\pi}{3}} \\ \mathcal{C}_3 : h_0(x) &\rightarrow h_0(C_3x); \eta(x) \rightarrow \eta(C_3x) - i\frac{\sqrt{3}}{3} \\ \mathcal{I} : h_0(x) &\rightarrow -h_0(-x); \eta(x) \rightarrow -\bar{\eta}(-x), \end{aligned} \quad (17)$$

where \mathcal{T}_1 and \mathcal{T}_2 are translation along $\vec{a}_1 = (\frac{\sqrt{3}}{2}, \frac{1}{2})$ and $\vec{a}_2 = (0, 1)$, \mathcal{C}_3 is the counterclockwise rotation by 120° , and \mathcal{I} is the inversion, both around center of the red plaquette. All the other lattice symmetries can be viewed as the combination of the above transformations. The transformation of h_0 and η are subject to $h^{r,g,b} \sim h^{r,g,b} + 3$, respectively, which we omit in the above to simplify the bookkeeping.

Hence, the vertex operators $\mathcal{V}_{\vec{m}}$ transforms under the following:

$$\begin{aligned} \mathcal{T}_1 : \mathcal{V}_{(m^r, m^g, m^b)}(x) &\rightarrow e^{-i\frac{2\pi}{3}(m^r + m^g + m^b)} \mathcal{V}_{(m^b, m^r, m^g)}(x) \\ \mathcal{T}_2 : \mathcal{V}_{(m^r, m^g, m^b)}(x) &\rightarrow e^{-i\frac{2\pi}{3}(m^r + m^g + m^b)} \mathcal{V}_{(m^g, m^b, m^r)}(x) \\ \mathcal{C}_3 : \mathcal{V}_{(m^r, m^g, m^b)}(x) &\rightarrow e^{-i\frac{2\pi}{3}(m^g - m^b)} \mathcal{V}_{(m^r, m^g, m^b)}(C_3x) \\ \mathcal{I} : \mathcal{V}_{(m^r, m^g, m^b)}(x) &\rightarrow \mathcal{V}_{(m^r, m^g, m^b)}^\dagger(-x). \end{aligned} \quad (18)$$

C. Effective field theory description

Taking into account the lattice symmetries, the effective 2+1D Lagragian at zero temperature can be written as,

$$\mathcal{L}[\theta_0, \vec{\vartheta}, h_0, \vec{\eta}] = \mathcal{L}_1[\theta_0, h_0] + \mathcal{L}_2[\vec{\vartheta}, \vec{\eta}] + \mathcal{L}_3[h_0, \vec{\eta}] + \dots, \quad (19)$$

where

$$\begin{aligned} \mathcal{L}_1[\theta_0, h_0] &= i\theta_0 \partial_\tau h_0 + \tilde{t}(\partial_\mu \theta_0)^2 + \tilde{v}_0(\partial_\mu h_0)^2 - \tilde{y}_0 \cos(2\pi h_0) \\ \mathcal{L}_2[\vec{\vartheta}, \vec{\eta}] &= i\vec{\vartheta} \cdot \partial_\tau \vec{\eta} + \tilde{t}'|\delta\vec{\vartheta}|^2 + \tilde{v}'(\partial_\mu \vec{\eta})^2 - \tilde{y}' \sum_i \cos(4\pi \vec{\alpha}_i \cdot \vec{\eta}) \\ \mathcal{L}_3[h_0, \vec{\eta}] &= -\tilde{y} \sum_i \cos[2\pi(h_0 + 2\vec{\alpha}_i \cdot \vec{\eta})]. \end{aligned} \quad (20)$$

Here, μ refers to two spatial coordinate to be summed over and $\delta\vec{\vartheta} \equiv \vec{\vartheta} - \langle \vec{\vartheta} \rangle$, where $\langle \vec{\vartheta} \rangle$ is obtained by minimizing Eq. 12. The cosine terms are present due to the compactness of $h^{r,g,b}$ fields, and we keep the lowest harmonics from combining $\mathcal{V}_{\vec{m}}$ ’s such that the lattice symmetries are satisfied. Here we introduce $\vec{\eta} = (\text{Re}[\eta], \text{Im}[\eta])$ and its corresponding conjugate field $\vec{\vartheta}$. The vectors $\alpha_{1,2,3} = (1, 0), (-\frac{1}{2}, \frac{\sqrt{3}}{2}), (-\frac{1}{2}, -\frac{\sqrt{3}}{2})$ are related by \mathcal{C}_3 rotation, where the lattice constant is 1. The cosine terms correspond to $\mathcal{V}_{(1,1,1)} + \text{h.c.}$, $\mathcal{V}_{(2,-1,-1)} + \text{h.c.} + (\text{cyclic permutation})$, and $\mathcal{V}_{(3,0,0)} + \text{h.c.} + (\text{cyclic permutation})$ in $\mathcal{L}_{1,2,3}$ respectively. The $(\partial_\mu \theta_0)^2$ originates from ring exchange terms such as \mathcal{O}_2 . The \dots denotes higher-order harmonics and gradient terms. What determines markedly different fates of h_0 and $\vec{\eta}$ is the fact that emergent global quantum number \tilde{N} requires the Lagragian to be invariant under $\theta_0 \rightarrow \theta_0 + \text{const}$ and hence forbids the θ_0^2 term, whereas $\delta\vec{\vartheta}^2$ term is allowed by symmetry.

After integrating out $\vec{\vartheta}$ in \mathcal{L}_2 , the action has the sine-Gordon form,

$$\mathcal{S}_{sg}[\eta] = \int \frac{1}{4\tilde{t}'^2} (\partial_\tau \vec{\eta})^2 + \tilde{v}'(\partial_\mu \vec{\eta})^2 - \tilde{y}' \sum_i \cos(4\pi \alpha_i \cdot \vec{\eta}). \quad (21)$$

Let us first ignore \mathcal{L}_3 . Then we have two decoupled sectors. It is well-known that the sine-Gordon theory in 2+1D has only a gapped phase, where $\vec{\eta}$ is pinned by the cosine terms. The same mechanism also explains the confinement of compact $U(1)$ gauge theory in 2+1D and the valence bond solid phases in quantum dimer models on a bipartite lattice in 2+1D [17]. Here, the two components of the $\vec{\eta}$ map to the two dual photon fields in the compact $U(1) \times U(1)$ gauge theory. With such $\vec{\eta}$ configurations, $\mathcal{L}_3 \rightarrow -3\tilde{y} \cos(2\pi h_0)$. Therefore, the effect of \mathcal{L}_3 is to renormalize \tilde{y}_0 to $\tilde{y}_0 + \tilde{y}$ in \mathcal{L}_1 to the leading order in \tilde{y}_0 .

Now let us focus on \mathcal{L}_1 , with $\tilde{y}_0 \rightarrow \tilde{y}_0 + \tilde{y}$. This theory can be mapped to the effective description of the 2+1D quantum XY model as follows. First, we apply the Villain approximation[28], which approximates the cosine

term with a sum of Gaussian functions centered around the integers and then integrates out the h_0 field. It is readily seen that

$$\mathcal{S}_1[\theta_0] = \int \frac{1}{\tilde{y}} (\partial_\tau \theta_0)^2 + \tilde{t} (\partial_\mu \theta_0)^2 + \dots, \quad (22)$$

where \tilde{y} is a monotonic function of $\tilde{y}_0 + \tilde{y}$. The Euclidean action $\mathcal{S}_1[\theta_0]$ also describes the 3D classical XY model with θ_0 as the spin azimuthal angle. By taking into account the vortices of θ_0 , there is a phase transition between a superfluid phase and a gapped Mott insulating phases by tuning the effective stiffness $K_{\text{eff}} = \sqrt{\tilde{t}/\tilde{y}}$ across a critical value K_{eff}^c [29]. Hence, there are two distinct phases:

- For $\tilde{t} < \tilde{y}(K_{\text{eff}}^c)^2$, $\langle h_0 \rangle \neq 0$, $\langle \eta \rangle \neq 0$: the gapped **columnar ordered phase**.
- For $\tilde{t} > \tilde{y}(K_{\text{eff}}^c)^2$, $\langle h_0 \rangle \neq 0$, $\langle \eta \rangle \neq 0$: the gapless **supernematic phase**.

We discuss the properties of each phase in the following sections.

V. COLUMNAR ORDERED PHASE

In the classical limit of $\tilde{t} = 0$, we reproduce the trimer liquid[13], a classical ensemble of extensively-many degenerate configurations (1 e)). In general, small quantum fluctuations around extensive degeneracy can result in quantum order-by-disorder, where a charge ordering state is favored due to the virtual exchange processes. To determine the symmetry-breaking pattern of such a charge-ordered state and its thermal behavior, we use the effective field theory and the symmetry representations of the fields.

A. Zero temperature

The order parameters of the columnar ordering phase are the lowest order vertex operators, with the following expectation values:

$$\begin{aligned} \langle \mathcal{V}_{(1,0,0)} \rangle &= e^{i\frac{2\pi}{3}(\bar{h}_0+e_1)} \\ \langle \mathcal{V}_{(0,1,0)} \rangle &= e^{i\frac{2\pi}{3}(\bar{h}_0+e_2)} \\ \langle \mathcal{V}_{(0,0,1)} \rangle &= e^{i\frac{2\pi}{3}(\bar{h}_0-e_1-e_2)}, \end{aligned} \quad (23)$$

where $\langle h_0 \rangle = \bar{h}_0$ and $\vec{\eta} = \left(\frac{e_1}{2}, \frac{\sqrt{3}}{3}(\frac{e_1}{2} + e_2)\right)$, where \bar{h}_0 , $e_{1,2}$ are integers. There are three distinct values for $\langle \mathcal{V}_{(1,0,0)} \rangle$ and we find $\langle \mathcal{V}_{(0,1,0)} \rangle$ respectively, and $\langle \mathcal{V}_{(0,0,1)} \rangle = \langle \mathcal{V}_{(1,0,0)} \rangle^* \langle \mathcal{V}_{(0,1,0)} \rangle^*$ from Eq.23. Therefore, there are nine distinct charge ordering phases in total, which correspond to the columnar ordering in Fig.1 c) and its symmetry-related counterparts. Physically, the $\langle \mathcal{V}_{(1,0,0)} \rangle$, $\langle \mathcal{V}_{(0,1,0)} \rangle$, and $\langle \mathcal{V}_{(0,0,1)} \rangle$ correspond to the order

parameter of the columnar ordering of the red, green, and blue double-dimers, respectively. The charge ordering gives rise to Bragg peaks at momentum $K_{CO} = \frac{4\pi}{3\sqrt{3}}(1, 0)$ and all the C_6 related momenta. The CO state is a “Mott-insulator” of \bar{N} that breaks lattice translational symmetry due to $\langle h_0 \rangle \neq 0$. It also breaks the threefold rotational symmetry of the lattice, C_3 , due to $\langle \vec{\eta} \rangle \neq 0$.

B. Finite temperature

To effective field theory Eq.20 can be extended to finite temperature. Deep in the CO phase, the effective action is a 2D sine-Gordon theory with three components,

$$S_{CO}[h_0, \eta] = \frac{1}{2} K_0 \int (\partial_\mu h_0)^2 + \frac{1}{2} K' \int (\partial_\mu \vec{\eta})^2 - \sum_{\vec{m}} y_{\vec{m}} \mathcal{V}_{\vec{m}}, \quad (24)$$

where $K_0 = 2\beta \tilde{v}_{0,\text{eff}}$, $K' = 2\beta \tilde{v}'_{\text{eff}}$. We note that, from Eq.20, for the ordering of h_0 , the corresponding cosine term is given by $\mathcal{V}_{(1,1,1)}$, whose scaling dimension is $\Delta_{(1,1,1)} = \frac{\pi}{K_0}$. For the ordering of $\vec{\eta}$, the corresponding term is $\mathcal{V}_{(2,-1,-1)}$, whose scaling dimension is $\Delta_{(2,-1,-1)} = \frac{4\pi}{K'}$. Hence, at low temperatures, all cosine terms are relevant around the Gaussian fixed point, leading to the CO.

To understand thermal melting of the CO we need to consider thermally excited violations of the cluster-charging interaction. A change in the occupation number at a single site violates three cluster-charging constraints associated with the three plaquettes sharing the site. Such excitation carries two effects as follows. (1) Violation of cluster-charging of a single plaquette generates “bionic” monomers, i.e., monomers of two colors of the height fields, as discussed for the classical trimer model at filling 1/3 [13]. The monomer charges of (h^r, h^g, h^b) -fields are $(0, 3, -3)$, $(-3, 0, 3)$ and $(3, -3, 0)$ for the bionic monomers residing in the red, green and blue plaquettes in Fig.5 b). Hence removing or adding one particle creates a bound state of three bionic monomers, where the total monomer charges sum to zero. (2) From the relation Eq.13, changing boson number of one single site corresponds to shifting h_0 by 1 after coarse-graining. The shift at site x_0 can be viewed as a “charge” of the \vec{h}_0 field and the configuration of h_0 satisfies $\nabla^2 h_0(x) = \delta^2(x - x_0)$. Hence, the scaling dimension of this shift operator is $\Delta_s = \frac{K_0}{4\pi}$, following the same argument as in the vortex operator in the XY model [30]. The critical K_0 for the shift is $K_{0,c} = 8\pi$ while the cosine term scales as $\Delta_{(1,1,1)}(K_{0,c}) = \frac{1}{8} < 2$ and is relevant. Hence, the thermal phase transition is dominated by the cosine term $\cos 2\pi h_0$ [31]. Since $h_0 \sim h_0 + 3$, the ordering of h_0 is three-fold degenerate, and we expect the thermal transition of h_0 to be three-state Potts-like.

In general, the ordering of h_0 and $\vec{\eta}$ do not coincide. The bionic monomers can be viewed as vortices of the $\vec{\eta}$ -field. Since the physical boson couples the shift in h_0

to the three-body bound state of the bionic monomers, the bionic monomers are always confined in the ordering phase of h_0 . This is because, to dissociate the bionic monomers, one needs to shift the value of h_0 along a line, yielding a linear energy cost. Therefore, when $\langle h_0 \rangle \neq 0$, the monomer fugacity for $\bar{\eta}$ is always zero at large distance. Hence, depending on the relative strength of K_0 and K' , there are two scenarios for the thermal melting of the CO, illustrated in Fig. 6:

(a) Upon increasing temperature, h_0 melts first, via a three-state Potts transition. The intermediate phase has $\vec{\eta}$ ordering. Since h_0 is disordered, the order parameters are the lowest order vertex operators involving only $\vec{\eta}$ -field: $\langle \mathcal{V}_{(1,-1,0)} \rangle$, $\langle \mathcal{V}_{(0,1,-1)} \rangle$ and $\langle \mathcal{V}_{(-1,0,1)} \rangle$. They all take the same value of $1, e^{i\frac{2\pi}{3}}$, or $e^{-i\frac{2\pi}{3}}$ from Eq.23. From Eq.18, the ordering pattern breaks \mathcal{C}_3 rotation while preserving translation and inversion. Hence, this intermediate phase is three-fold degenerate, which we call “nematic”. In the disordered phase of h_0 , the bionic monomers can acquire non-zero fugacity. The scaling dimension of these monomer operators can be obtained from the same method as in the classical trimer liquid [13] and $\Delta_{m_n} = \frac{3K'}{4\pi}$. Hence when $K' = K'_c = \frac{8\pi}{3}$, the monomers start to become relevant. However, since $\Delta_{(2,-1,-1)}(K'_c) = \frac{3}{2} < 2$, the thermal phase transition is dominant by the cosine terms, where the value of the critical K' is nonuniversal, and expected to be three-state Potts like [31].

(b) Upon increasing temperature, $\vec{\eta}$ melts first while h_0 is ordered. Since the bionic monomers have zero fugacity in the ordering phase of h_0 , the melting of $\vec{\eta}$ is driven by the cosine terms becoming irrelevant, which happens at $K' \equiv K'_{\text{lower}} = 2\pi$ (lower boundary of the magenta region in Fig.6 b)). Above this temperature, the effective theory of $\vec{\eta}$ is Gaussian and critical. This phase has C_6 rotation symmetry and the three-sublattice translation breaking induced by $\langle h_0 \rangle$ is quasi-long range, which we call “plaquette Coulomb phase”. Further increases in temperature cause the three-state Potts transition of melting h_0 . Since the bionic monomer at most has scaling dimension $\frac{3K'_{\text{lower}}}{4\pi} = \frac{3}{2} < 2$, the Coulomb phase terminates at the thermal melting transition of h_0 , where bionic monomers proliferate, and the stiffness K'_{upper} right below the transition (upper boundary of the magenta region in Fig.6 b)) can related to the lower boundary of the PC phase as $K'_{\text{upper}} = 2\pi T_1/T_2$, where $T_{1,2}$ are the lower and upper temeprature of the PC phase, from the Gaussian field theory.

VI. SUPERNEMATIC

A. Zero temperature

The low-energy description above establishes SN as a “superfluid” of sublattice particle number $\tilde{N} = N_A - N_B$, the new quantum number for the cluster-charging model

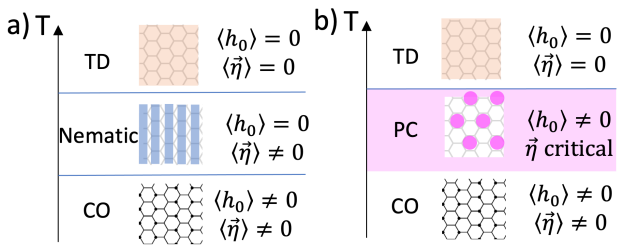


FIG. 6. Two scenarios of the thermal phase transition of the Columnar order, with the cartoon picture denoting the ordering patterns. The nematic order breaks C_3 while preserving translation and inversion. PC: palquette Coulomb, $\sqrt{3} \times \sqrt{3}$ quasi-long range ordering while preserving C_6 rotation. TD: thermally disordered. The blue lines denote a three-state Potts transition. The magenta region denotes quasi-long range order.

based on the Conway-Lagarias invariant. From the perspective of the quantum number \tilde{N} , properties of SN should follow from well-known properties of a superfluid. However, total particle number $N = N_A + N_B$ is gapped, rendering SN incompressible. Hence, SN is an unusual new state of matter that is macroscopically coherent, yet incompressible. Moreover, since the tiling invariant \tilde{N} cannot be changed locally, the order parameter defined on the lattice has to be nonlocal. The SN has a unique “intertwined order” that breaks the global $U(1)$ symmetry associated with \tilde{N} conservation due to $\langle \theta_0 \rangle \neq 0$ and three-fold rotation C_3 due to pinning of $\vec{\eta}$ as we show below.

Since h_0 is fluctuating in the SN, the lowest order vertex operators $\mathcal{V}_{(1,0,0)}$'s do not acquire expectation values, which means that each single color in the double-dimer model is not ordered. However, the joined configuration of different colors might have ordering due to the pinning of the η -field. To address this question, we consider vertex operators involving only $\vec{\eta}$ -fields. The lowest order operators are $\mathcal{V}_{(1,-1,0)}$, $\mathcal{V}_{(0,1,-1)}$, and $\mathcal{V}_{(-1,0,1)}$. All the other $\vec{\eta}$ -only vertex operators can be generated by considering the complex conjugation and multiplication of the above ones. The vertex operator $\mathcal{V}_{(1,-1,0)}$ corresponds to the multiplication of the dimer densities of the neighboring red and green dimers, similarly for the $\mathcal{V}_{(0,1,-1)}$, and $\mathcal{V}_{(-1,0,1)}$. The expectation values of these vertex operators are:

$$\begin{aligned}\langle \mathcal{V}_{(1,-1,0)} \rangle &= e^{i \frac{2\pi}{3}(e_1 - e_2)} \\ \langle \mathcal{V}_{(0,1,-1)} \rangle &= e^{i \frac{2\pi}{3}(e_1 + 2e_2)} \\ \langle \mathcal{V}_{(-1,0,1)} \rangle &= e^{i \frac{2\pi}{3}(-2e_1 - e_2)},\end{aligned}\tag{25}$$

where $\vec{\eta} = \left(\frac{e_1}{2}, \frac{\sqrt{3}}{3} \left(\frac{e_1}{2} + e_2 \right) \right)$, the same as in the CO case. We note that $\langle \mathcal{V}_{(1,-1,0)} \rangle = \langle \mathcal{V}_{(0,1,-1)} \rangle = \langle \mathcal{V}_{(-1,0,1)} \rangle$, and can take value of $1, e^{i\frac{2\pi}{3}}$, or $e^{-i\frac{2\pi}{3}}$. This ordering breaks \mathcal{C}_3 but preserves inversion and translation. Hence, we can label the SN phase at zero temperature by two

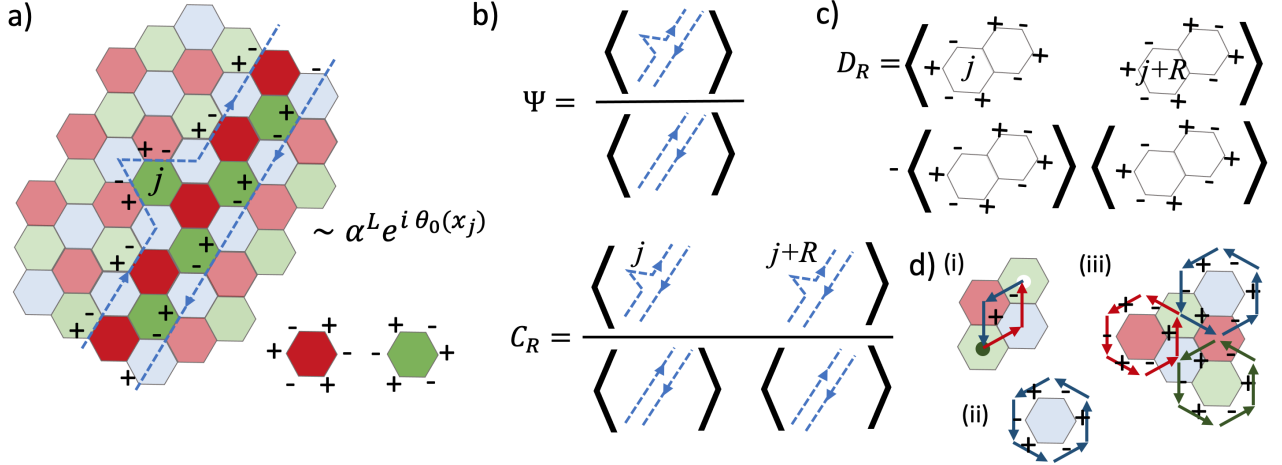


FIG. 7. a) Example of a charged operator under $N_A - N_B$. The \pm denote creation and annihilation operators of the particles, and the arrows denote two different assignments of the consecutive \pm 's. Note that we have colored the honeycomb plaquette with three colors and demand that the double loops consist of lines traversing plaquettes of the same color (blue in the figure). Bottom: sign assignment for the red and green plaquettes. b) Order parameter and off-diagonal long-range order defined on the lattice. c) Connected correlator of \mathcal{O}_2 's with separation R . d) (i) Bionic monomer hopping from the green plaquette to another green one. (ii) Single plaquette flipping process assisted by the presence of one bionic monomer. (iii) Lowest order symmetry breaking process involving only θ_0 -fields at finite temperature. The solid and hollow circles denote increasing and decreasing monomer numbers, respectively. The colored arrows denote the gauge field capturing the Gauss Law of the cluster-charging constraints.

order parameters, $\langle e^{i\theta_0} \rangle$ and $\langle \mathcal{V}_{(1,-1,0)} \rangle$. Since $\theta_0 \rightarrow -\theta_0$ under inversion, the SNs with $\langle e^{i\theta_0} \rangle = \pm 1$ are inversion symmetric, and are otherwise inversion breaking.

As a “superfluid” of \tilde{N} , the SN has a gapless Goldstone mode with the corresponding dynamical structure that is linear in q . Specifically, we can express the particle density in terms of the coarse grained fields,

$$n_A(x) - \frac{1}{3} = -n_B(x) + \frac{1}{3} \sim -\frac{1}{2\pi} \sin 2\pi h_0 + \dots, \quad (26)$$

where we ignore the dependence on the gapped η -fields and a spatially oscillating term (see SM A3 for the derivation). Following the effective field theory of θ_0 (Eq.22) and the standard derivation following the hydrodynamic theory of bosonic superfluid [32] (see SM B), the dynamical structure factor $\tilde{S}(q, \omega) \sim |q|\delta(\omega - v|q|)$, where $\tilde{S}(q, \omega) = \int dt e^{i\omega t} \langle \tilde{n}(q, t) \tilde{n}(-q, 0) \rangle$, and $\tilde{n}(q)$ is the Fourier transform of $n_A(x_A) - n_B(x_B)$. Therefore, the SN is compressible with respect to the sublattice particle number \tilde{N} , following the compressibility sum-rule [33] $\tilde{\kappa} = 2 \lim_{q \rightarrow 0} \int_0^\infty \frac{\tilde{S}(q, \omega)}{\omega} d\omega$. Hence, from the \tilde{N} perspective, SN is compressible although it is an incompressible state for the total particle number $N = N_A + N_B$.

Despite the seeming resemblance of the effective field theory of the SN Eq. (22), to that of a typical superfluid, the SN carries the fingerprint of its unusual microscopic origin tied to the global CL tiling invariant through a *non-local* order parameter. Unlike an ordinary superfluid, the SN has no local order parameter because \tilde{N} is exactly conserved, i.e. a local operator charged under \tilde{N} is forbidden. Instead, we find a non-local string

operator that carries \tilde{N} charge and reduces to the local field $e^{i\theta_0}$ in the long-wavelength limit. To construct this charged string operator, first consider a single hexagonal plaquette that hosts a height field. An operator consisting of alternating creation and annihilation operators around this plaquette (the green plaquette in Fig. 7a)) changes the corresponding height by 3 (and hence changes \tilde{N}), but annihilates all states in the constrained Hilbert space, because it demands three particles on one plaquette. However, we can stay within the constrained Hilbert space by considering an extended operator that stitches plaquettes supporting two of the three height-field colors (say red and green) along a non-contractible loop (Fig. 7a)). Adding one extra hexagon – the “bump” – to this extended operator ensures a net change in \tilde{N} . The resulting operator is supported on two oppositely oriented lines connecting blue plaquettes (blue dashed lines in Fig. 7a)), where the orientation tracks the ordering of creation and annihilation operators. [34]

Although this \tilde{N} -charged operator is loop-like, the \tilde{N} symmetry differs fundamentally from the 1-form symmetry in gauge theories: the \tilde{N} charge of the double-loop depends on its shape, in contrast to the Wilson loop in gauge theory, whose charge depends only on topological data. In the continuum, a double-loop with a bump around plaquette x_j matches $\alpha^L e^{i\theta_0(x_j)}$ to leading order, where L is the string length and α is a non-universal perimeter-law factor arising from integrating out the gapped η sector (and from the short-distance contribution to $e^{i \oint \nabla \theta \cdot d\ell}$). We can define a normalized expectation value of the “bump” operator, Ψ , as the ra-

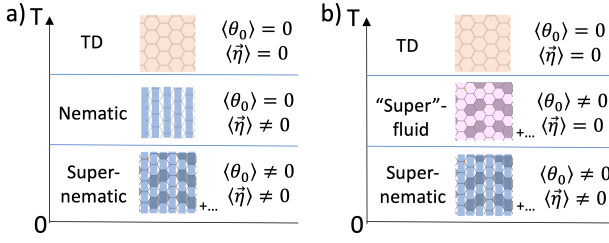


FIG. 8. Two scenarios of the thermal phase transition of the super-nematic phase, with the cartoon picture denoting the ordering patterns. TD: thermally disordered. The blue lines denote three-state Potts transition.

tio between the expectation values of the double loop with and without the bump, as shown in Fig. 7 b). We also define an analogously normalized “bump” correlation function for the “bump”s separated by distance R , C_R . Now one can detect the SN phase by observing a nonzero Ψ under infinitesimal symmetry breaking and by a finite C_R at large separation R . This corresponds to a *non-local*, off-diagonal, long-range order (ODLRO). In finite-size simulations, connected correlators of local operators, such as density or \mathcal{O}_2 (Fig. 7c), decay as a power law in the SN phase but exponentially in the charge-ordering phase, providing a practical diagnostic.

B. Finite temperature

At finite temperature, the \tilde{N} symmetry is no longer exact, since thermally activated bosonic hopping between the A and B sublattices allows local processes that change \tilde{N} . The central question is therefore whether the finite-temperature phase of the SN can still be viewed as a *superfluid* of \tilde{N} , despite the presence of these thermally induced violations. To address this, we derive the leading \tilde{N} -breaking terms generated by thermal fluctuations.

In the imaginary-time path-integral language, the thermal partition function can be written as,

$$Z = \text{Tr } e^{-\beta H} \sim \int \mathcal{D}[\theta_0, \vec{\eta}, m_\alpha] e^{-S_E[\theta_0, \vec{\eta}, m_\alpha]}, \quad (27)$$

where m_α denotes the monomer fields, to be specified later. We decompose the action as $S_E[\theta_0, \vec{\eta}, m_\alpha] = S_0[\theta_0, \vec{\eta}] + S_{\text{viol}}$, where S_0 is the thermal action for the constrained Hilbert space and S_{viol} denotes the contribution from the thermal violation of the cluster-charging constraints.

S_0 is governed by the effective action obtained by taking the classical limit of our quantum effective theory (ignoring the τ -dependent terms in Eqs. 21 and 22),

$$S_0[\theta_0, \vec{\eta}] = \int d^2x \left(\frac{1}{2} \rho_0 (\partial_\mu \theta_0)^2 + \frac{1}{2} K' (\partial_\mu \vec{\eta})^2 - \sum_{\vec{m}} y_{\vec{m}} \mathcal{V}_{\vec{m}} \right), \quad (28)$$

where $\rho_0 = 2\beta\tilde{t}$ is the phase stiffness, and $\mathcal{V}_{\vec{m}}$ denotes the vertex operators. The $\vec{\eta}$ sector is described by a two-component sine-Gordon theory identical to that in the CO phase (Eq. 24).

S_{viol} consists of two contributions: the monomer hopping term and the cluster-charging energy,

$$S_{\text{viol}} = \int_0^\beta d\tau \sum_{\alpha, i, j} -t m_{\alpha, i}^\dagger e^{i(A_{ij}^\delta - A_{ij}^\gamma)} m_{\alpha, j} + \sum_{\alpha, i} U m_{i, \alpha}^\dagger m_{i, \alpha}. \quad (29)$$

Here we only consider monomer hopping terms mapped to the boson hopping between nearest neighbors, $-tb_i^\dagger b_j$. The higher-order hopping terms can be written in a similar way. $m_{\alpha, i}$ denotes the annihilation operator for a “bionic” monomer residing at plaquette center i , and $\alpha, \delta, \gamma = r, g, b$ label the color indices (see Fig. 7 d)(i)) with the following rule. A monomer $m_{g, i}$ located on a green plaquette violates the cluster constraint on that plaquette and, consequently, the dimer constraints on both the red and blue bonds in the corresponding dimer representation, similarly for $m_{r, i}$ and $m_{b, i}$. Interpreting the dimer constraints as Gauss laws, $m_{g, i}$ carries opposite gauge charges under the emergent fields A^r and A^b (defined on different links as shown in Fig. 7 d)(i)), realizing the “bionic” character introduced in Ref. [13]. The magnetic flux defined by summing the gauge fields A_{ij}^α around a hexagonal plaquette centered at site l is related to the conjugate height field as $\sum_{\langle ij \rangle \in \square_l} A_{ij}^\alpha = 3\theta_l^\alpha$.

The effect of thermally generated monomers can be captured by integrating over all possible monomer configurations. This procedure yields gauge-invariant combinations of the link fields A_{ij} ’s, corresponding to ring-exchange processes mediated by virtual monomer excitations. Owing to the bionic nature of the monomers, the lowest-order gauge-invariant process necessarily involves three successive monomer hoppings around a hexagon, resulting in a three-particle flip on a single plaquette (Fig. 7d)(ii)), which generates the term

$$-w_1 e^{-\beta U} \sum_{\alpha=\{r,g,b\}} \sum_l \cos(3\theta_l^\alpha), \quad (30)$$

where $w_1 \sim O(t^3/U^2)$, and the Boltzmann factor $e^{-\beta U}$ accounts for the probability that plaquette l hosts three particles, enabling the flip to occur.

Eq.30 explicitly breaks \tilde{N} conservation since it is not invariant under constant shift of θ_0 . The question now is whether it destroys the SN phase at zero temperature. $\theta^{\alpha=r,g,b}$ ’s are linear combinations of θ_0 and $\vec{\vartheta}$ fields. In the ordered phase of $\vec{\eta}$, the fields $\vec{\vartheta}$ are pinned. They acquire expectation values that minimize Eq. 12. The minima satisfy $(3\theta^r - 3\theta^g, 3\theta^g - 3\theta^b, 3\theta^b - 3\theta^r) = 2\pi(n_1, n_2, -n_1 - n_2)$ with integers $n_{1,2}$, corresponding to $(\vartheta_x, \vartheta_y) = 2\pi(-n_2/\sqrt{3}, (2n_1 + n_2)/3)$. Pinning of the $\vec{\vartheta}$ fields induces cosine terms in θ_0 via the assisted single-plaquette flip (Eq. 30). This term is relevant in the superfluid phase of \tilde{N} , and its minima satisfy

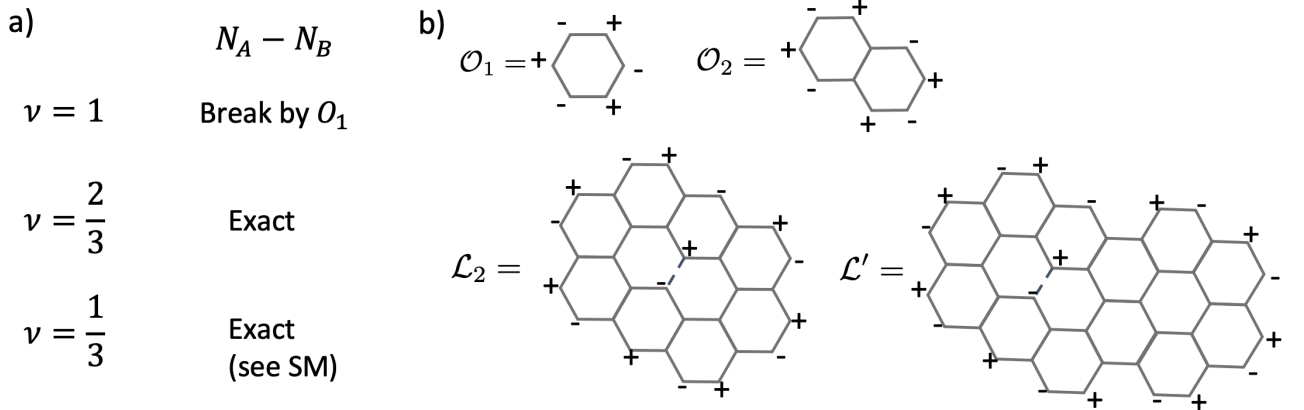


FIG. 9. a) The presence or absence of the $\tilde{N} = N_A - N_B$ conservation. Here exact means present upto all local operators. b) Some non-zero ring exchange operators. \mathcal{O}_1 , \mathcal{O}_2 and \mathcal{L}_2 are the lowest order operators for filling $1, 2/3$ and $1/3$ respectively. \mathcal{L}_2 also conserves the dipole moment of \tilde{N} , which is broken by higher order operators such as \mathcal{L}' .

$\cos(\theta_0 + 2\pi(2n_1 + n_2)/3) = 1$ for $t > 0$. However, summing over all degenerate vacua of the $\vec{\eta}$ ordering—i.e., all integer pairs (n_1, n_2) —renders θ_0 effectively a random angle that can be any integer multiples of $2\pi/3$. On average, Eq. 30 therefore does not fix θ_0 .

To capture the leading term that directly couples to θ_0 , we consider ring-exchange processes independent of $\vec{\vartheta}$. The dominant contribution is a three-plaquette process (Fig. 7d)(iii)) that produces a threefold anisotropy,

$$-w_3 e^{-3\beta U} \int d^2x \cos(3\theta_0), \quad (31)$$

with $w_3 \sim O(t^9/U^8)$. This term explicitly breaks the \tilde{N} symmetry and pins $e^{i\theta_0}$ to one of the three minima: 1, $e^{i2\pi/3}$, or $e^{-i2\pi/3}$.

Therefore, the ordering of the phase angle θ_0 is discrete and long-ranged, characterized by a Z_3 order. The connected two-point correlator exhibits a finite correlation length, distinguishing the thermal phase of the SN from a genuine superfluid phase of \tilde{N} in the thermodynamic limit. Nevertheless, the effect of the threefold anisotropy can remain weak over a large length scale, owing to the small Boltzmann factor $e^{-3\beta U}$ and the high-order hopping amplitude w_3 . The length scale beyond which the anisotropy becomes relevant defines a pinning length l_p . Within the range of l_p , the thermal SN phase effectively behaves as a superfluid of \tilde{N} . To leading order in w_3 , the pinning length is estimated from the renormalization group analysis[30] as,

$$l_p \sim (w_3^{-1} e^{3\beta U})^{\frac{1}{2-\Delta_3}} > e^{3\beta U/2}, \quad (32)$$

where $\Delta_3 = 9/(4\pi\rho_0)$ is the scaling dimension of the $\cos(3\theta_0)$ operator. Despite the explicit anisotropy, the exponential factor ensures that l_p can remain exceedingly large. For instance, at $T/U \sim 0.1$, the pinning length exceeds 10^6 lattice spacings, indicating that the

zero-temperature discussion based on exact \tilde{N} conservation remains effectively valid even at finite temperature.

Now let us discuss the thermal melting of the SN. Because both θ_0 and $\vec{\eta}$ order in SN, it can melt in two ways (Fig.8). A two-stage melting proceeds via an intermediate phase whose nature depends on which order melts first: a) if θ_0 disorders while $\vec{\eta}$ remains ordered, the intermediate phase is nematic that breaks \mathcal{C}_3 but preserves translation; b) if $\vec{\eta}$ disorders first but θ_0 retains Z_3 phase coherence, we call the intermediate phase “super”-fluid due to the phase coherence. Since $\cos(3\theta_0)$ is relevant at the would-be BKT transition of a true \tilde{N} superfluid [31], we expect that thermal transition of θ_0 to be three-state Potts-like. Therefore, in either route, both transitions, between SN and the intermediate phase, and between the intermediate and the fully disordered phase, are in the three-state Potts universality class, reflecting Z_3 symmetry breaking at each step.

VII. OTHER FILLINGS

Extending beyond $\nu = 2/3$, the cluster constraint $\sum_{i \in \mathcal{O}_r} n_i \in \{0, 1, 2, 3, 4, 5, 6\}$ yields the “commensurate” fillings $\nu = 0, 1/3, 2/3, 1, 4/3, 5/3, 2$. Since ν and $2 - \nu$ are related by particle-hole symmetry and $\nu = 0$ is trivial, it suffices to analyze $\nu = 1/3, 2/3$ and 1 . At $\nu = 1/3$, Thm. 1 applies directly (no need for the tile set Σ_2), so \tilde{N} remains an exact symmetry of the constrained Hilbert space. In contrast, at $\nu = 1$ the leading ring exchange breaks \tilde{N} (Fig. 9a). A constructive scheme (see SM Sec. C) can be proved to generate all local operators order by order, yielding the leading ring exchanges (Fig. 9b) to be \mathcal{O}_1 for $\nu = 1$, \mathcal{O}_2 for $\nu = 2/3$, and \mathcal{L}_2 (the “Lemniscate operator” in Ref.[12]) for $\nu = 1/3$. Notably, \mathcal{L}_2 conserves a sublattice dipole $\tilde{P} = \sum_i n_A(x_i) \vec{x}_i - \sum_j n_A(x_j) \vec{x}_j$, which is violated by

higher-order terms such as \mathcal{L}' . Therefore we also expect the SN phase to exist at $\nu = 1/3$. For $\nu = 1$, the \mathcal{O}_1 term gaps the system into a sublattice charge-ordered state.

VIII. SUMMARY AND DISCUSSION

In summary, we uncovered a robust mechanism by which geometric frustration and local Hilbert-space constraints enforce an emergent, globally conserved quantum number for bosons under cluster charging interaction on the honeycomb lattice. By mapping the constrained Hilbert space at $\frac{2}{3}$ ($\frac{4}{3}$) or $\frac{1}{3}$ ($\frac{5}{3}$) filling to a nontrivial tiling problem and invoking the Conway–Lagarias boundary invariant, we rigorously established global conservation of the sublattice polarization $\tilde{N} = N_A - N_B$, beyond the previously shown $U(1) \times U(1)$ gauge symmetry of classical ground state[13]. By mapping the local constraints to coupled double-dimers, we derive an effective field theory that faithfully incorporates the conservation of \tilde{N} and the local constraints of the bosonic quantum Hamiltonian. Quantum fluctuations within this manifold give rise to an insulating yet macroscopically phase-coherent and gapless “supernematic” (SN) phase, characterized by a unique intertwined order that spontaneously breaks both the emergent global $U(1)$ symmetry and the lattice C_3 rotation, but not translation. We derived a *non-local* order parameter representing the SN that can be detected through ODLOR: the “bumped loop” operator, which is markedly different from familiar Wilson loop through its shape-dependent charge under \tilde{N} . Furthermore, we showed that the quantum phase transition between the columnar-ordered Mott insulator and the SN phase belongs to the 3D XY universality class. We also analyzed the finite temperature transitions that sequentially restore the broken symmetries.

The proposed SN phase is unusual in many ways as a phase of matter. (i) It is a gapless insulator. (ii) It is a macroscopically phase-coherent state that is not a superfluid. (iii) It is an intertwined order with C_3 breaking (nematic) that originates from the elongated resonance operators. (iv) It has a non-local order parameter that is distinct from the more familiar Wilson loop for its charge being shape-dependent. Naturally, it will be most exciting to realize SN in physical systems. Although our field-theoretic discussion only holds for bosonic systems, the conservation of \tilde{N} due to Conway–Lagarias invariant at filling $1/3$ and $2/3$ of the quantum cluster-charging model is independent of statistics. Since the charged object under \tilde{N} responsible for the condensation is bosonic in both bosonic and fermionic models, we expect that the SN could still be present in a fermionic trimer model, which we leave for future studies.

While explicit derivation of the critical value for the microscopic parameters of the original Hamiltonian is beyond the reach of the effective field theory, a concrete microscopic model for realizing the SN phase will be a trimer variant of the so-called Rokhsar–Kivelson Hamil-

tonian, dubbed the trimer–Rokhsar–Kivelson (trimer-RK) Hamiltonian. This model is a natural generalization of the RK Hamiltonian introduced for quantum dimer models [5]. The trimer-RK Hamiltonian includes both a ring-exchange term, \mathcal{O}_2 , and a potential term (see Appendix E for the explicit form). At the RK point, where the strengths of these two terms are equal, the ground state is an equal-weight superposition of all trimer-covering configurations, analogous to the dimer model at its RK point. In dimer models on bipartite lattices, such as the honeycomb lattice [35], perturbations away from the RK point toward stronger exchange terms drive the system into an ordered phase. In contrast, quantum fluctuations around the trimer-RK point generate an effective action that stabilizes the SN phase (see Appendix E). The key distinction between the proposed trimer-RK and dimer-RK Hamiltonians is rooted in the \tilde{N} invariance. In the trimer case, the dynamics including stochastic fluctuations must preserve \tilde{N} exactly, leading to a Langevin equation of the same form as that describing volume-conserving surface growth [36]. Upon quantization, this yields the phase-angle Lagrangian identical to Eq. 22, in contrast to the quantum Lifshitz model that governs the dimer RK point on bipartite lattices [37].

As a physical platform to pursue the realization of SN, we propose the Rydberg atom array. The Rydberg blockade mechanism has been shown to provide cluster-charging constraints on honeycomb lattices [38]. The algebraic decay of various operators of the SN phase can be directly measured in this platform. Measuring the non-local order parameter can be challenging, but it may be achievable through strategies analogous to that used for topological phases in Ref. [39]. Since the total number of particles is not fixed in Rydberg systems, we need to consider the stability of the SN under doping away from the commensurate fillings ($2/3$ or $1/3$). As was discussed in the thermal violation of \tilde{N} conservation, the monomers induce a threefold anisotropy, which pins the macroscopic phase angle of the SN. Doping also introduces monomers that carry fractionalized charges of $e/3$ [12, 13]. However, since the $\vec{\eta}$ field is pinned in the SN phase, we expect these monomers to be confined at low temperature and to become deconfined only in the “super”-fluid regime at finite temperature.

Our unprecedented use of tiling invariants to discover a new quantum many-body state opens a new path for quantum-state preparation to approach a classically hard problem: the tiling combinatorial optimization problem. While we have focused on a specific set of tiles, it would be interesting to explore whether the notion of a boundary invariant extends to other tilings or to other lattices. An open question is whether the operator \mathcal{O}_2 is ergodic in the Hilbert space of configurations satisfying local constraints, or whether geometrical constraints generate hidden conserved quantities beyond \tilde{N} and the 1-form symmetries. Physical realization of coherent superpositions of trimer configurations would provide a powerful means to probe such questions, offering direct access to

the structure of constrained Hilbert spaces where ergodicity may break down. More broadly, these simulations could shed light on the quantum dynamics underlying hard combinatorial optimization problems, where quantum interference could provide a speedup over classical methods.

Acknowledgement. – DM thanks Jiaxin Qiao, Yizhi You, Cenke Xu, Yi-Zhuang You, Jing-Yuan Chen, Zheng-Cheng Gu, T. Senthil for the stimulating discussions.

We thank Christopher Mudry and Eduardo Fradkin for feedbacks on the draft. DM is supported by SNSF Grant No. 219339. E-AK was supported in part by the NSF through the grant OAC-2118310 supported by the U.S. Department of Energy through Award Number: DE-SC0023905. This research is funded in part by the Gordon and Betty Moore Foundation’s EPiQS Initiative, Grant GBMF10436 to E-AK and grant NSF PHY-2309135 to the Kavli Institute for Theoretical Physics (KITP).

[1] E. Wigner, Phys. Rev. **46**, 1002 (1934).

[2] N. F. Mott, Proceedings of the Physical Society. Section A **62**, 416 (1949).

[3] C. Castelnovo, R. Moessner, and S. L. Sondhi, Nature **451**, 42 (2008).

[4] R. Moessner, S. L. Sondhi, and E. Fradkin, Physical Review B **65**, 024504 (2001).

[5] D. S. Rokhsar and S. A. Kivelson, Phys. Rev. Lett. **61**, 2376 (1988).

[6] A. Kitaev, Annals of Physics **321**, 2 (2006), january Special Issue.

[7] R. Moessner and S. L. Sondhi, Phys. Rev. Lett. **86**, 1881 (2001).

[8] K. Zhang, Y. Zhang, L. Fu, and E.-A. Kim, Communications Physics **5**, 250 (2022).

[9] A. Verberkmoe and B. Nienhuis, Phys. Rev. Lett. **83**, 3986 (1999).

[10] J. Conway and J. Lagarias, Journal of Combinatorial Theory, Series A **53**, 183 (1990).

[11] G. Giudice, F. M. Surace, H. Pichler, and G. Giudici, Physical Review B **106**, 195155 (2022).

[12] D. Mao, K. Zhang, and E.-A. Kim, Physical Review Letters **131**, 106801 (2023).

[13] K. Zhang, D. Mao, E.-A. Kim, and R. Moessner, Bionic fractionalization in the trimer model of twisted bilayer graphene (2024), arXiv:2410.00092 [cond-mat.str-el].

[14] M. P. A. Fisher, P. B. Weichman, G. Grinstein, and D. S. Fisher, Physical Review B **40**, 546 (1989).

[15] S. Elitzur, Physical review d **12**, 3978 (1975).

[16] S. Sachdev, Phys. Rev. B **45**, 12377 (1992).

[17] A. Polyakov, Nuclear Physics B **120**, 429 (1977).

[18] E. Fradkin and S. H. Shenker, Phys. Rev. D **19**, 3682 (1979).

[19] A recently established powerful perspective for understanding the radical difference observes that the local resonating operator preserves a $U(1)$ 1-form symmetry associated with the winding number of the dimers in the bipartite lattice, while only a Z_2 1-form symmetry in the non-bipartite lattice. (see e.g. Ref.[40, 41] and the reference therein).

[20] R. Kenyon, Communications in Mathematical Physics **326**, 477 (2014).

[21] H. Blote and H. Hilhorst, Journal of Physics A: Mathematical and General **15**, L631 (1982).

[22] B. Nienhuis, H. J. Hilhorst, and H. Blote, Journal of Physics A: Mathematical and General **17**, 3559 (1984).

[23] N. Wilkins and S. Powell, Phys. Rev. B **102**, 174431 (2020).

[24] A. Paramekanti, L. Balents, and M. P. A. Fisher, Physical Review B **66**, 054526 (2002).

[25] N. E. Myerson-Jain, S. Liu, W. Ji, C. Xu, and S. Vijay, Physical Review Letters **128**, 115301 (2022).

[26] E. Fradkin, D. A. Huse, R. Moessner, V. Oganesyan, and S. L. Sondhi, Physical Review B **69**, 224415 (2004).

[27] E. Fradkin, *Field theories of condensed matter physics* (Cambridge University Press, 2013).

[28] J. Villain, Journal de Physique **36**, 581 (1975).

[29] K. G. Wilson and M. E. Fisher, Phys. Rev. Lett. **28**, 240 (1972).

[30] J. M. Kosterlitz and D. J. Thouless, Journal of Physics C: Solid State Physics **6**, 1181 (1973).

[31] J. V. José, L. P. Kadanoff, S. Kirkpatrick, and D. R. Nelson, Phys. Rev. B **16**, 1217 (1977).

[32] V. N. Popov, *Functional Integrals and Collective Excitations*, Cambridge Monographs on Mathematical Physics (Cambridge University Press, 1988).

[33] L. Pitaevskii and S. Stringari, in *Bose-Einstein Condensation and Superfluidity* (Oxford University Press, 2016).

[34] The presence of the boundary invariant requires particular care when taking the thermodynamic limit. Under periodic boundary conditions, the total number of unit cells along one direction must be a multiple of three to realize the exact commensurate fillings and to define the charged loop operator. For open boundaries, the edges must be softened to enable access to different \tilde{N} sectors, and the charged operator would be touching the boundary.

[35] R. Moessner, S. L. Sondhi, and P. Chandra, Phys. Rev. B **64**, 144416 (2001).

[36] T. Sun, H. Guo, and M. Grant, Phys. Rev. A **40**, 6763 (1989).

[37] C. L. Henley, Journal of Physics: Condensed Matter **16**, S891 (2004).

[38] M. Kornjača, R. Samajdar, T. Macrì, N. Gemelke, S.-T. Wang, and F. Liu, Communications Physics **6**, 358 (2023).

[39] G. Semeghini, H. Levine, A. Keesling, S. Ebadi, T. T. Wang, D. Bluvstein, R. Verresen, H. Pichler, M. Kalinowski, R. Samajdar, A. Omran, S. Sachdev, A. Vishwanath, M. Greiner, V. Vuletić, and M. D. Lukin, Science **374**, 1242 (2021).

[40] R. Kobayashi, K. Shiozaki, Y. Kikuchi, and S. Ryu, Phys. Rev. B **99**, 014402 (2019).

[41] S. D. Pace and X.-G. Wen, Physical Review B **108**, 195147 (2023).

[42] C. L. Henley, Journal of Statistical Physics **89**, 483 (1997).

[43] G. Parisi and Y. S. Wu, Sci. sin **24**, 483 (1981).

[44] R. Dijkgraaf, D. Orlando, and S. Reffert, Nuclear Physics B **824**, 365 (2010).

Appendix A: Details on symmetry properties of the height fields

1. Colomnar ordering states

For the dimer models on bipartite lattice, the “flat” height field configurations of the coarse-grained heights are the columnar ordering. For the double-dimer model on the honeycomb lattice of our interest, there are two possible colomnar ordering: the ones with double occupation (Fig. 10 a)) Eand the ones with loops (Fig. 10 b)). However, when mapping back to physical particle configurations, the colomnar ordering with double occupation violates the cluster-charging constraints at filling 2/3 because some plaquettes are forced to host three particles. Hence we will only consider the colomnar ordering with loops in the following.

There are three distinct columnar orderings related by lattice translation for one color. Naively, there are $3^3 = 27$ columnar orderings taking into account the three colors. However, there are only 9 of them that can be mapped to physical configurations, one of which listed in Fig. 10 c) with the height fields. The other COs can be related to the one in Fig. 10 c) by lattice translation and rotation.

2. Symmetry properties under lattice transformations

Microscopically, the height fields transform under the lattice symmetries as the following,

$$\begin{aligned} \mathcal{T}_1 : h^{r,g,b}(x) &\rightarrow h^{g,b,r}(T_1 x) \\ \mathcal{T}_2 : h^{r,g,b}(x) &\rightarrow h^{b,g,r}(T_2 x) \\ \mathcal{C}_3 : h^{r,g,b}(x) &\rightarrow h^{r,g,b}(C_3 x) \\ \mathcal{I} : h^{r,g,b}(x) &\rightarrow -h^{r,g,b}(-x), \end{aligned} \quad (\text{A1})$$

where the center of the C_3 rotation and inversion is taken to be around the center of a red plaquette.

In the continuum, the coarse-graining introduces non-zero average values of $h^{r,g,b}$, and the lattice symmetry can act with some additional shift on top of the microscopic translation [26]. To see this clearly, we consider the nine colomnar ordering states (flat configurations with constant average colored height fields). The lattice transformation among these COs can be implemented via applying local operators across the lattice, allowing us to derive the values of height fields starting from one specific CO (see Fig.11). Hence, under lattice symmetries,

the average heights transform as such,

$$\begin{aligned} \mathcal{T}_1 : \tilde{h}_0 &\rightarrow \tilde{h}_0 - 1; \tilde{\eta} \rightarrow \tilde{\eta} e^{-i\frac{4\pi}{3}} \\ \mathcal{T}_2 : \tilde{h}_0 &\rightarrow \tilde{h}_0 - 1; \tilde{\eta} \rightarrow \tilde{\eta} e^{i\frac{4\pi}{3}} \\ \mathcal{C}_3 : \tilde{h}_0 &\rightarrow \tilde{h}_0; \tilde{\eta} \rightarrow \tilde{\eta} - i\frac{\sqrt{3}}{3} \\ \mathcal{I} : \tilde{h}_0 &\rightarrow -\tilde{h}_0; \tilde{\eta} \rightarrow -\tilde{\eta}, \end{aligned} \quad (\text{A2})$$

where

$$\begin{aligned} \tilde{h}^r &= \tilde{h}_0 + \tilde{\eta} + \tilde{\eta}^* \\ \tilde{h}^g &= \tilde{h}_0 + \tilde{\eta} e^{-i\frac{4\pi}{3}} + \tilde{\eta}^* e^{i\frac{4\pi}{3}} \\ \tilde{h}^b &= \tilde{h}_0 + \tilde{\eta} e^{i\frac{4\pi}{3}} + \tilde{\eta}^* e^{-i\frac{4\pi}{3}}. \end{aligned} \quad (\text{A3})$$

Here we use $\tilde{\cdot}$ to denote the avearge value of the height fields around three sublattices of each color.

Adding up the shift in the average heights and the microscopic transformation gives us the transformation of the height fields in the continuum, namely, Eq.17.

3. Relating coarse-grained fields to microscopic fields

Recall Eq. 13, microscopically,

$$n_A = -\frac{1}{3} \sum_{\triangleright} h + \frac{1}{3}, \quad n_B = \frac{1}{3} \sum_{\triangleleft} h + \frac{1}{3}. \quad (\text{A4})$$

If we perform a gradient expansion of the above equations, we obtain $\partial\eta$ terms to the leading order,

$$n_A - \frac{1}{3} \sim -e^{-i\frac{2\pi}{3}(2n_2+n_1)}(\partial_x + i\partial_y)\eta + h.c. + \dots, \quad (\text{A5})$$

where we denote the coordinate of n_A as $n_1\vec{a}_1 + n_2\vec{a}_2 \equiv (x_A, y_A)$. $\vec{a}_1 = (\frac{\sqrt{3}}{2}, \frac{1}{2})$ and $\vec{a}_2 = (0, 1)$ are the lattice vectors. The prefactor has the three sublattice structure corresponding to the three different r, g, b height fields positions around a given A site. The similar contribution in n_B can be written as,

$$n_B - \frac{1}{3} \sim e^{-i\frac{2\pi}{3}(2n_2+n_1)}(\partial_x - i\partial_y)\eta + h.c. + \dots, \quad (\text{A6})$$

Note that in the gradient expansion, there is also a term that is propotional to h_0 . Since h_0 is a compact field, we should find a vertex operator that has the same behavior around small h_0 , which is the $\mathcal{V}_{(1,1,1)}$. This contributes to n_A and n_B as,

$$\begin{aligned} n_A - \frac{1}{3} &\sim -\frac{1}{2\pi} \sin 2\pi h_0 \\ n_B - \frac{1}{3} &\sim \frac{1}{2\pi} \sin 2\pi h_0 \end{aligned} \quad (\text{A7})$$

However, this is not the full story due to the smearing in the coarse-graining. To the leading order in vertex operator, this amounts to match the lattice configuration

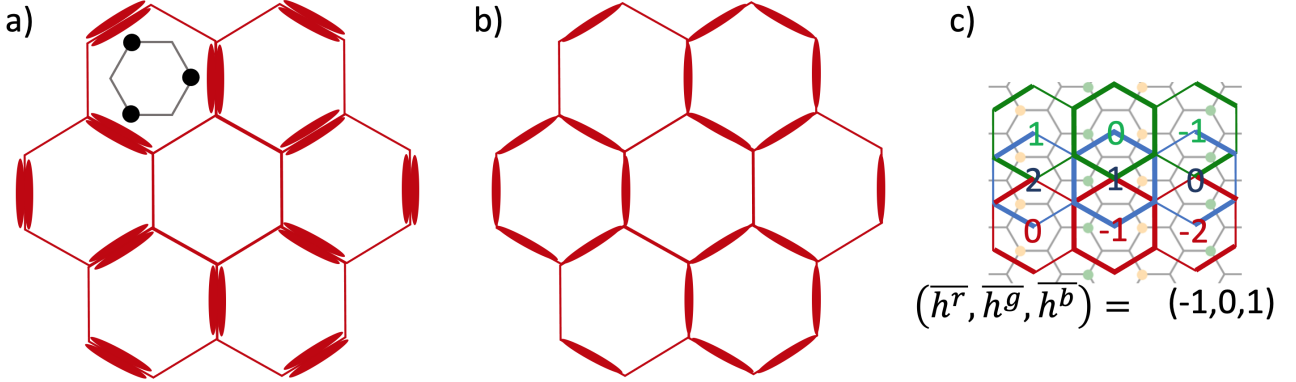


FIG. 10. Two possible types columnar orders in the honeycomb lattice double-dimer model. a) With double occupation, the corresponding physical configuration has three particles of some plaquettes, violating cluster-charging constraints at filling 2/3. One of such plaquette configurations is labelled by the black dots. b) Columnar orders with loops around the honeycomb plaquettes. c) The columnar order of the physical configuration (in the background) and the corresponding columnar orders of the three double-dimer models (only the three consecutive plaquettes are shown), with the corresponding height fields. The height fields of each color has the three sublattice structure. Bottom : the average of the height fields of the three sublattices of each color.

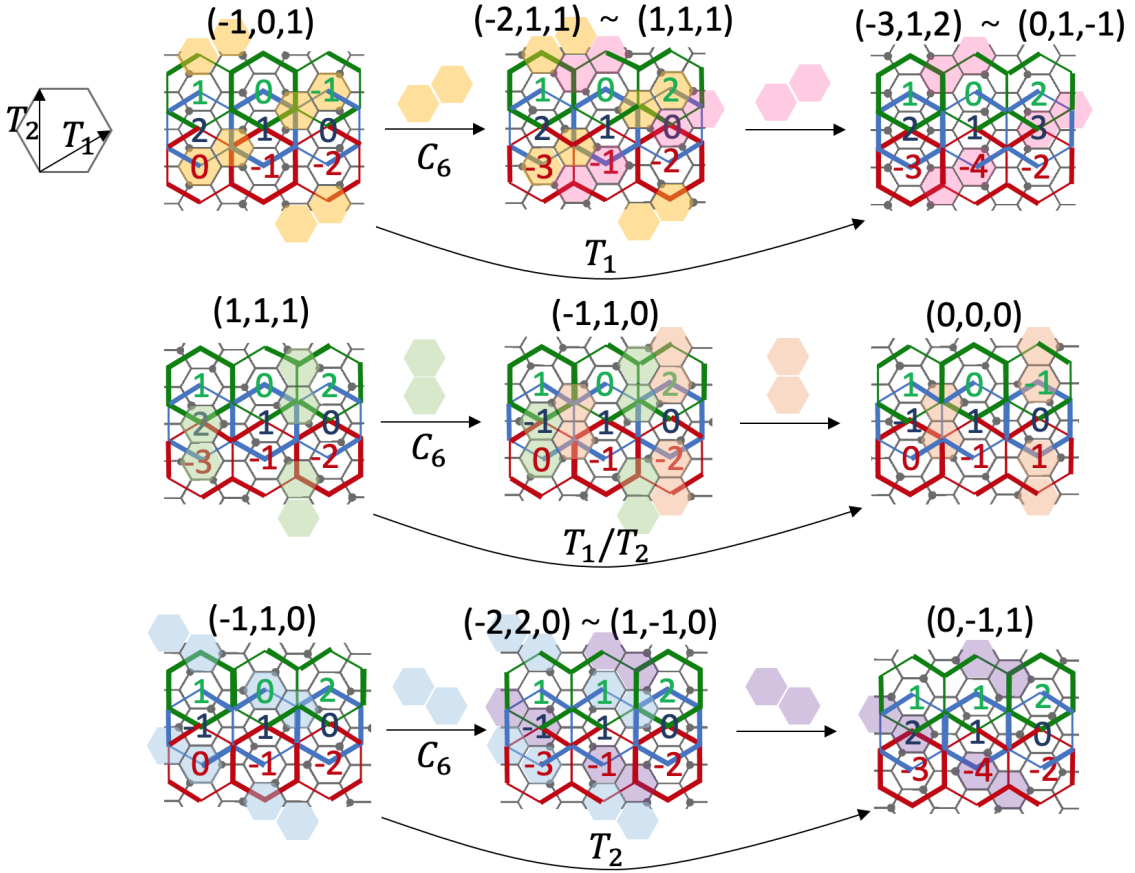


FIG. 11. Change of height under applying local operators. Upperleft: definition of lattice translations. For each CO, the three numbers above denote the $(\tilde{h}^r, \tilde{h}^g, \tilde{h}^b)$, taking average over the heights of the three sublattices of the corresponding color (colored numbers in the center of the plaquettes). Note that we only present the dimer configuration and heights of three plaquettes but the pattern is repeated periodically. The shaded double plaquette denotes where a \mathcal{O}_2 (or \mathcal{O}_2^\dagger) is applied, which matches the symbols above the arrows, denoting the “before” and “after” applying of the operator. The corresponding lattice transformation is denoted underneath the arrow. We also note that each $(\tilde{h}^r, \tilde{h}^g, \tilde{h}^b)$ is defined mod 3. Here we only present seven out of nine COs but the transformation of the rest can be worked out in the similar fashion.

of the columnar ordering and the corresponding uniform heights in the continuum, analogous to dimer model [26], which yields,

$$\begin{aligned}
n_A - \frac{1}{3} & \sim \frac{1}{9} \left[e^{i\frac{2\pi}{3}(\frac{x_A}{\sqrt{3}}+y_A)-i\frac{2\pi}{3}} (e^{i\frac{2\pi}{3}h^r} + e^{i\frac{2\pi}{3}h^g} + e^{i\frac{2\pi}{3}h^b}) \right] \\
& + \frac{1}{9} \left[e^{-i\frac{2\pi}{3}\frac{2x_A}{\sqrt{3}}-i\frac{2\pi}{3}} (e^{i\frac{2\pi}{3}h^r} + e^{i\frac{2\pi}{3}h^g-i\frac{2\pi}{3}} + e^{i\frac{2\pi}{3}h^b+i\frac{2\pi}{3}}) \right] \\
& + \frac{1}{9} \left[e^{-i\frac{2\pi}{3}(-\frac{x_A}{\sqrt{3}}+y_A)-i\frac{2\pi}{3}} (e^{i\frac{2\pi}{3}h^r+i\frac{2\pi}{3}} + e^{i\frac{2\pi}{3}h^g-i\frac{2\pi}{3}} + e^{i\frac{2\pi}{3}h^b}) \right] \\
& + h.c.,
\end{aligned} \tag{A8}$$

where $h^{r,g,b}$ have the corresponding coordinates according to the microscopic relation Eq.A4.

Plugging in the pinned values for $\vec{\eta}$, we have,

$$n_A - \frac{1}{3} \sim \frac{1}{9} e^{i\frac{2\pi}{3}h_0(x_A)} \sum_{\alpha} f_{\alpha}(x_A) + h.c., \tag{A9}$$

where the summation is taken over the r, g, b heights around the site x_A , denoted by α , and the factors $f_{\alpha}(x_A)$ can be written as,

$$\begin{aligned}
f_r &= e^{i\frac{2\pi e_1}{3}} \left(e^{iG_1 \cdot r_A - i\frac{2\pi}{3}} + e^{iG_2 \cdot r_A - i\frac{2\pi}{3}} + e^{iG_3 \cdot r_A} \right) \\
f_g &= e^{i\frac{2\pi e_2}{3}} \left(e^{iG_1 \cdot r_A - i\frac{2\pi}{3}} + e^{iG_2 \cdot r_A + i\frac{2\pi}{3}} + e^{iG_3 \cdot r_A + i\frac{2\pi}{3}} \right) \\
f_b &= e^{\frac{-i2\pi(e_1+e_2)}{3}} \left(e^{iG_1 \cdot r_A - i\frac{2\pi}{3}} + e^{iG_2 \cdot r_A} + e^{iG_3 \cdot r_A - i\frac{2\pi}{3}} \right),
\end{aligned} \tag{A10}$$

where $G_1 = \frac{2\pi}{3}(\frac{1}{\sqrt{3}}, 1)$, $G_2 = \frac{2\pi}{3}(-\frac{2}{\sqrt{3}}, 0)$, and $G_3 = \frac{2\pi}{3}(\frac{1}{\sqrt{3}}, -1)$.

Similarly, for sublattice B,

$$\begin{aligned}
n_B - \frac{1}{3} & \sim \frac{1}{9} \left[e^{i\frac{2\pi}{3}(\frac{x_B}{\sqrt{3}}+y_B)+i\frac{2\pi}{9}} (e^{i\frac{2\pi}{3}h^r} + e^{i\frac{2\pi}{3}h^g} + e^{i\frac{2\pi}{3}h^b}) \right] \\
& + \frac{1}{9} \left[e^{-i\frac{2\pi}{3}\frac{2x_B}{\sqrt{3}}+i\frac{2\pi}{9}} (e^{i\frac{2\pi}{3}h^r} + e^{i\frac{2\pi}{3}h^g-i\frac{2\pi}{3}} + e^{i\frac{2\pi}{3}h^b+i\frac{2\pi}{3}}) \right] \\
& + \frac{1}{9} \left[e^{-i\frac{2\pi}{3}(-\frac{x_B}{\sqrt{3}}+y_B)+i\frac{2\pi}{9}} (e^{i\frac{2\pi}{3}h^r+i\frac{2\pi}{3}} + e^{i\frac{2\pi}{3}h^g-i\frac{2\pi}{3}} + e^{i\frac{2\pi}{3}h^b}) \right] \\
& + h.c..
\end{aligned} \tag{A11}$$

where the origin of the coordinate systems is set to be at A site. We also have,

$$n_B - \frac{1}{3} \sim \frac{1}{9} e^{i\frac{8\pi}{9}} e^{i\frac{2\pi}{3}h_0(x_B)} \sum_{\alpha} f_{\alpha}(x_B) + h.c.. \tag{A12}$$

To summarize, in terms of the coarse-grained fields, to the leading orders, there are three contributions to the density $n_{A,B}$: a $\partial\eta$ term (Eq. A4), a $\sin 2\pi h_0$ term (Eq. A7) and a $e^{i\frac{2\pi}{3}h_0}$ term with spatially periodic coefficients (Eq. A9).

Appendix B: Sublattice density structure factor

Before integrating out the h_0 field in the effective action of the phase angle θ_0 in Eq.22, we have

$$\mathcal{S}_1[h_0, \theta_0] = \int -ih_0 \partial_{\tau} \theta_0 + \frac{\tilde{\mathbf{y}}}{4} h_0^2 + \tilde{t}(\partial_{\mu} \theta_0)^2 + \tag{B1}$$

From the equation of motion of h_0 ,

$$h_0 = \frac{i2\partial_{\tau} \theta_0}{\tilde{\mathbf{y}}}. \tag{B2}$$

Hence, in Matsubara frequency, the correlation function of h_0 in momentum space is,

$$\chi_{h_0}(q, i\omega_n) = \frac{4}{\tilde{\mathbf{y}}^2} \omega_n^2 \chi_{\theta_0} = \frac{2}{\tilde{\mathbf{y}}} \frac{\omega_n^2}{\omega_n^2 + v^2 q^2}, \tag{B3}$$

where $v = \sqrt{\tilde{\mathbf{y}}}$ is the velocity of the Goldstone mode.

Analytic continuation $i\omega_n \rightarrow \omega + i0^+$ of χ_{h_0} gives the retarded Green's function $\chi_{h_0}^R(q, \omega)$. The dynamical structure factor $S(q, \omega)$ follows from the fluctuation-dissipation theorem. At zero temperature,

$$S(q, \omega) = \frac{-\Theta(\omega)}{\pi} \text{Im}\{\chi_{h_0}^R(q, \omega)\} = \frac{v|q|}{\tilde{\mathbf{y}}} \delta(\omega - v|q|), \tag{B4}$$

and the static structure factor $S(q) = \int d\omega S(q, \omega)$.

Now let us consider the structure factor of the sublattice density $\tilde{n}(q) \equiv \sum_i n_{i,A} e^{iq \cdot x_{i,A}} - \sum_j n_{j,B} e^{iq \cdot x_{j,B}}$. From Eq.A7, A9 and A12, we can write $\tilde{n}(q)$ in terms of h_0 fields. It is readily seen that

$$\begin{aligned}
\tilde{n}(q, \omega) &\sim A \frac{v|q|}{\tilde{\mathbf{y}}} \delta(\omega - v|q|) \\
& + B \sum_i \frac{v|q + G_i|}{\tilde{\mathbf{y}}} \delta(\omega - v|q + G_i|) \text{ for } q \rightarrow 0,
\end{aligned} \tag{B5}$$

where $G_{i=1,2,3} = G_{1,2,3}$ defined in Eq.A10 and $G_{i=4,5,6} = -G_{1,2,3}$, and A, B are some constants. In the above equation, the first term comes from correlation between $\sin(2\pi h_0)$ and the second term from the ones between $e^{i\frac{2\pi}{3}h_0} f_{\alpha}(x)$.

Appendix C: Systematic construction of local operators

Here we give a systematic construction of a set of local operators that commutes with the cluster charging constraints, denoted as \mathbb{S}_{op} . We then prove that the set of nonzero local operators at a particular filling fraction, denoted as \mathbb{S}_{op-nz} , is always a subset of \mathbb{S}_{op} . To construct the set of local operators, we first consider how to represent the configurations in a manner that is convenient for comparing the difference between them. It turns out that the relationship between the particle number and

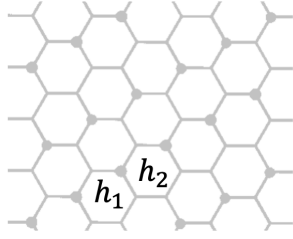


FIG. 12. Gauge choice for the height fields.

the height field (Eq.13) can be generalized to filling 1 and $1/3$,

$$n_A = -\frac{1}{3} \sum_{\triangleright} h + \frac{\nu}{2}, \quad n_B = \frac{1}{3} \sum_{\triangleleft} h + \frac{\nu}{2}. \quad (\text{C1})$$

For a given particle configuration n_i 's, the mapping to height fields is not one-to-one, namely, gauge redundancy in Eq.C1. We can fix the gauge by fixing the value of the height fields corresponding to two different colors. For instance, we can choose to fix h_1 and h_2 to be constant integers in Fig. 12. After the gauge-fixing, the mapping between the n_i configuration and the height field is injective, using Eq.C1, and the cluster-charging condition is satisfied by construction. Therefore, it is readily seen that the following lemma hold,

Lemma 1. *For two configurations with the same ν , satisfying cluster-charging condition, differ locally, their height field representations also differ locally after gauge fixing.*

Therefore, we can construct all the possible local operators for n_i 's if we can find a way to construct local operators for h_j 's. We denote the set of local operators in the height representation as \mathbb{S}_{op} . The construction is in the following subsection.

However, the mapping between particle number configuration and the height configuration is not surjective. Since Eq.C1 only ensure that integer-valued n_i 's maps to integer-valued h_j 's, given fixed integer $h_{1,2}$, it does not exclude the possibility that some configuration of h_j 's can map back to “unphysical” n_i 's, such as non-integer values or negative values, despite satisfying the cluster-charging condition. In particular, there are operators which we call “zero operators” that are local in the height representation but annihilate all the physical particle configurations. We will discuss those zero operators in the subsection after the next. Hence the set \mathbb{S}_{op} is strictly larger than the set of the physical local operators acting on n_i 's, denoted as \mathbb{S}_{op-nz} , which are the subset containing “non-zero” operators.

1. Local operators in \mathbb{S}_{op}

Now let us consider the effect of local operators on the height fields defined in the previous section. From

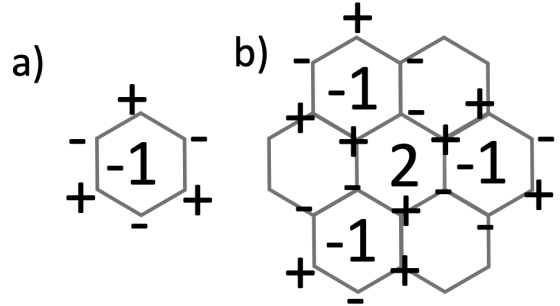


FIG. 13. Local operators constructed from $\Delta h/3$.

Lemma 1, the local operator in n_i 's changes h_j fields locally, which we denote as Δh . Due to the relationship Eq.C1, the minimal change in the height is $\Delta h = \pm 3$.

Let us consider $\Delta h_r = -3$ for plaquette r . By definition, it means that around plaquette r , the occupations on A sublattice decrease by 3 and those on B sublattice increase by 3, which is precisely the action of operator \mathcal{O}_1 (Fig. 13 a)).

Since $\Delta h/3$ can be any integer, the operator can also have “strength” other than 1. This does not make sense by itself since we cannot annihilate/create a particle more than once due to hard core constraints. However, such $\Delta h/3$ pattern can still make sense after taking into account the nearby plaquettes as long as the change in the resulting n_i fields is still ± 1 or 0. See Fig.13 b) for an example.

Since all the local operators can be viewed as local patterns of $\Delta h/3$ fields and all the $\Delta h/3$ patterns can be viewed as stacking and combining the \mathcal{O}_1 's, we obtain a systematic way of constructing all the possible local operators.

2. Zero operators

In the previous section, we derive a systematic construction of the set \mathbb{S}_{op} . Now we will show that there are the so-called “zero operators” in \mathbb{S}_{op} , which annihilate all the states in the constrained physical Hilbert space at a certain filling ν .

Here we give some examples of zero operators (Fig.14). The obvious type of zero operators is that it has more + (or -) signs around a plaquette than what the filling fraction imposes, such as \mathcal{O}_1 for filling $2/3$ and \mathcal{O}_2 for filling $1/3$. However, there are more subtle zero operators, such as \mathcal{O}_3 and \mathcal{Y} for filling $2/3$ and $\mathcal{L}_{1,d}$ for filling $1/3$. So far, we are only able to tell that these are zero operators by considering the particle configurations upon which they act non-vanishingly and finding a contradiction to the imposed filling fraction.

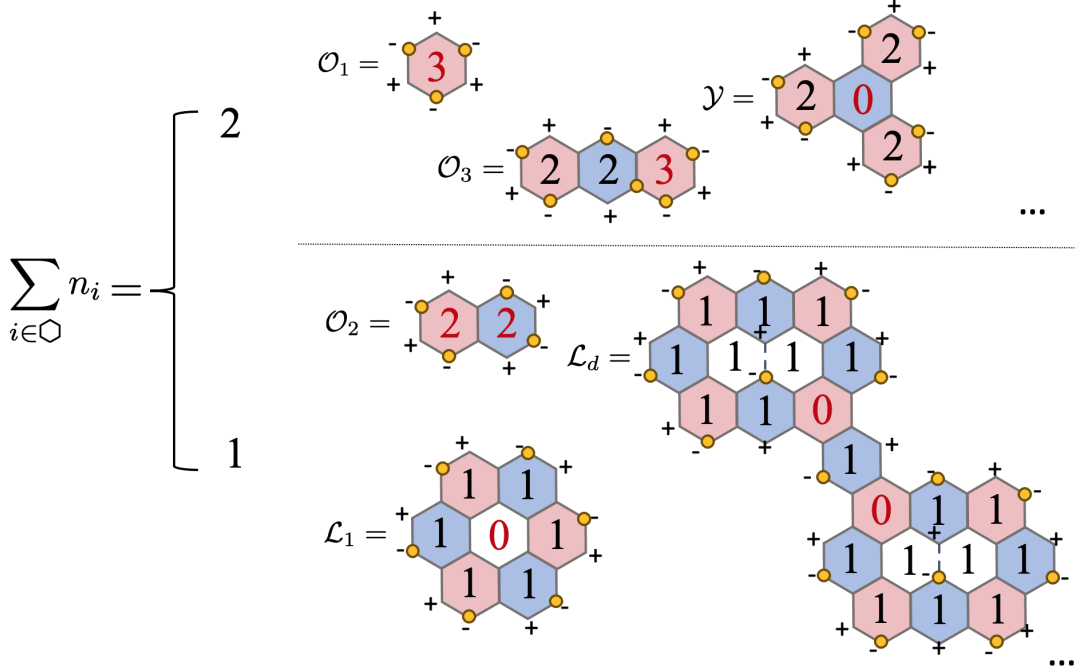


FIG. 14. Examples of zero operators for filling $2/3$ and $1/3$. The color pink and blue denote \mathcal{O}_1 with strength ± 1 . The numbers on the plaquette denote the sum of the particle numbers around it, which enables the corresponding operator to act non-vanishingly. In particular, the red number denotes the contradiction with the filling constraints.

Appendix D: Tile mapping and quantum number for filling $1/3$

For filling $1/3$, there is a one-to-one correspondence between a charge configuration and a tiling pattern of a triangular tiles on honeycomb lattice (Fig.15 a)), where the particles on the sites of the honeycomb lattice are denoted as black dots in the center of the tiles. The particle on the A (B) sublattice of the honeycomb lattice is mapped to tile T_1 (T_2) and the cluster charging constraint is satisfied by the tiling conditions that there is no gap or overlap allowed between the tiles. Therefore, applying Thm. 1, we find that for any tilable region R with a boundary ∂R , (see Fig.15 b) for an example of R), the difference of the sublattice particle number within R , i.e., $(N_A - N_B)_R \equiv \sum_{i \in R} (n_{i,A} - n_{i,B})$ only depends on the “shape” of the boundary, i.e., the word generated by ∂R . Therefore via the same logic as in the filling $2/3$ case, \tilde{N} is a conserved quantity under any action of local operators.

We note that the mapping from particles to tiles in the case of filling $1/3$ cannot be applied directly to filling $2/3$. The reason is that if we map the particle to tiles as in Fig.15 a), we have overlapping tiles, i.e. each hexagonal plaquette gets touched twice by the tiles. For such overlapping tiling configurations, there is no direct generalization of Thm. 1 since the overlapping tiling cannot always be separated as two regular tilings with no overlaps and no gaps. In the main text, we overcome this difficulty by creating another mapping that maps

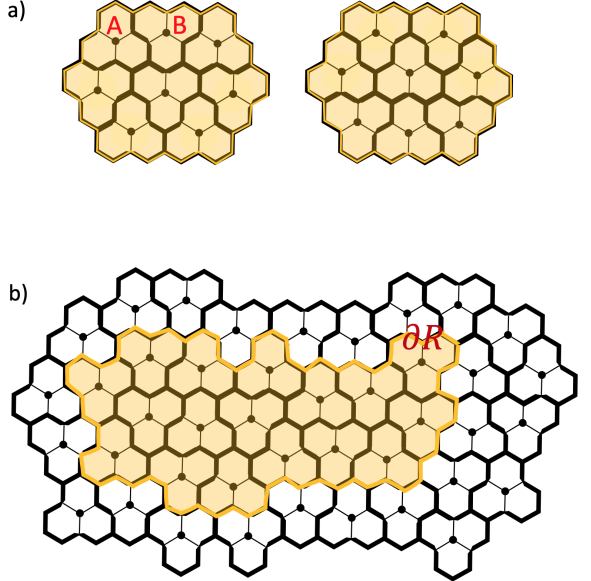


FIG. 15. a) Mapping between the particles on A and B sublattices (black dots) and the tiles (three cojoining hexagonal plaquettes) and the corresponding tiling pattern for the before and after states upon the action of the lemniscate operator \mathcal{L}_2 . The orange shades denote the area within which the tiles rearrange. b) An example of a region R (orange shade), with boundary ∂R (orange contour).

the constraints for filling 2/3 to yet another nonoverlapping tiling problem, with edge matching puzzles as the building block.

Appendix E: Perturbing around trimer-RK point

In the quantum dimer model on bipartite lattice, the dimer constraints can be viewed as Gauss law on the sites of the lattices [26], and the low-energy physics can be described by compact $U(1)$ gauge theory in $2+1D$. The quantum fluctuation of the local moves in the dimer model corresponds to the instanton events and leads to confinement. Therefore, the gapless RK point is in general unstable under quantum fluctuation. We can ask the analogous question for the trimer model, that is, starting from the trimer RK point where the wavefunction is an equal weight superposition of all possible classical trimer configuration, what is the role of quantum fluctuation?

For simplicity let us focus on filling 2/3. The trimer-RK Hamiltonian can be written as,

$$H_{t\text{-RK}} = -t \sum_{i,\alpha} (\mathcal{O}_2^\alpha(x_i) + h.c.) + V \sum_{i,\alpha} \mathcal{P}^\alpha(x_i), \quad (\text{E1})$$

where $\mathcal{P}^\alpha(x_i)$ is the potential term and α denotes its orientation (see Fig.16 for one orientation). The RK point

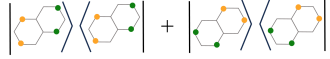


FIG. 16. Potential term \mathcal{P}

of the Hamiltonian $H_{t\text{-RK}}$ is when $t = V$, at which the ground state is an equal weight superposition of all possible particle configurations at filling 2/3, subject to the cluster-charging constraints. For each topological sector with fixed N and fixed $U(1) \times U(1)$ winding numbers, there is one such state.

Now we would like to derive the effective action, perturbing away from the RK point. We do so by first considering the height field representation. As pointed out in the main text, the $h^{R,G,B}$ fields can be recast into h_0 and $\vec{\eta}$ fields. Classically, the entropy functional takes a Gaussian form of the fluctuation around the flat configuration. For dimer models on bipartite lattice, this yields $e^{-\int (\partial_\mu h)^2}$, since the dimer density is $\sim \partial h$. However, as noted in Sec. A 3, in the relationship between the density and the heights, $\vec{\eta}$ and h_0 enter differently. Roughly speaking, we have $n \sim e^{iKx} \partial \eta + \sin h_0$. Hence the entropy functional $S_{cl} = S_{cl}[\vec{\eta}] + S_{cl}[h_0]$, where

$$S_{cl}[\vec{\eta}] = \frac{1}{2} K_\eta (\partial_\mu \vec{\eta})^2, \quad (\text{E2})$$

and

$$S_{cl}[h_0] = m h_0^2. \quad (\text{E3})$$

The coefficient K_η can be obtained by matching the Gaussian action of the classical trimer model in Ref. [13].

In the dimer model near RK point, it was realized by Henley [37, 42] that in the long wavelength limit, the plaquette flip dynamics can be captured by a Langevin equation of the height field (similar technique is also under the name of ‘‘stochastic quantization’’, see [43, 44] and the reference therein). Let us only focus on the h_0 field. The dynamics of h_0 follows the following Langevin equation,

$$\partial_\tau h_0(\vec{r}, \tau) = -f[h_0] + \zeta(\vec{r}, \tau), \quad (\text{E4})$$

where $f[h_0] = \frac{\delta S_{cl}[h_0]}{\delta h_0} = 2m h_0$. $\zeta(\vec{r}, \tau)$ is a noise term, which we will specify later.

In dimer model with plaquette flipping dynamics, $\zeta(\vec{r}, \tau)$ is taken to be a Gaussian white-noise. However, this is no longer the case for the dynamics of $h_0(\vec{r}, \tau)$. Since any local operator conserves the the total height, the dynamics should preserve $\sum_{\vec{r}} h_0(\vec{r}, \tau)$ at any given τ , including the noise term $\zeta(\vec{r}, \tau)$. As a result, we demand $\zeta(\vec{r}, \tau) = \nabla \cdot \vec{\xi}(\vec{r}, \tau)$, where $\xi_{x,y}(\vec{r}, \tau)$ are two independent Gaussian white-noise field. Therefore, taken into account the rotation symmetry of the lattice, the noise $\zeta(\vec{r}, \tau)$ satisfy,

$$\begin{aligned} \langle \zeta(\vec{r}, \tau) \rangle &= 0 \\ \langle \zeta(\vec{r}, \tau) \zeta(\vec{r}', \tau') \rangle &= -2D \nabla^2 \delta^2(\vec{r} - \vec{r}') \delta(\tau - \tau'), \end{aligned} \quad (\text{E5})$$

which is of the same form as in volume conserving surface growth dynamics[36].

Therefore, the Lagrangian that give rise to the trajectory can be written as,

$$\begin{aligned} \mathcal{L} = & -(\partial_\tau h_0 + 2m h_0) \frac{1}{D \nabla^2} (\partial_\tau h_0 + 2m h_0) \\ & - \alpha \cos(2\pi h_0) - \beta (\nabla h_0)^2 + \dots, \end{aligned} \quad (\text{E6})$$

where the α , β and \dots terms denote the terms perturbing away from the RK point. The first term in the above Lagrangian reproduces the noise correlation given by Eq. E5.

Let us perform a Hubbard-Stratonovich (HS) decomposition of the first term and,

$$\begin{aligned} \mathcal{L}[\theta, h_0] = & i\theta (\partial_\tau h_0 + 2m h_0) + \frac{D}{4} (\nabla \theta)^2 \\ & - \alpha \cos(2\pi h_0) - \beta (\nabla h_0)^2 + \dots \end{aligned} \quad (\text{E7})$$

By dimensional analysis, the scaling dimension of h_0 is 3/2, which makes a h_0^2 term marginal and a $(\nabla h_0)^2$ irrelevant. Near the minima of the cosine term, we can expand to the quadratic order in h_0 , since higher orders are irrelevant. Then integrating out h_0 we have,

$$\mathcal{L}[\theta] = \frac{1}{8\pi^2 \alpha} [(\partial_\tau - 2m)\theta]^2 + \frac{D}{4} (\nabla \theta)^2, \quad (\text{E8})$$

We then redefine $\theta_0 = \theta e^{-2m\tau}$ and rescale the τ direction to get ,

$$\mathcal{L}[\theta_0] = \frac{1}{8\pi^2 \alpha} (\partial_\tau \theta_0)^2 + \frac{D}{4} (\nabla \theta_0)^2, \quad (\text{E9})$$

matching the effective action in the main text for the SN phase for small quantum fluctuation parametrized by α .

From symmetry analysis, the potential term in $H_{t\text{-RK}}$ can be identified with the \mathcal{L}_3 term in Eq.20 to the leading

order. To get the SN phase, we need a flat configuration for the $\vec{\eta}$ -fields, which requires $t > V$. The pinning of the $\vec{\eta}$ would then lead to the $\cos(2\pi h_0)$ term.